minerals

MDPI

Article

Mechanism of Biomineralization Induced by *Bacillus subtilis* J2 and Characteristics of the Biominerals

Zuozhen Han [1,2,*], Jiajia Wang [1], Hui Zhao [3,*], Maurice E. Tucker [4,5], Yanhong Zhao [1], Guangzhen Wu [1], Jingxuan Zhou [3], Junxiao Yin [6], Hucheng Zhang [3], Xinkang Zhang [1] and Huaxiao Yan [1,3,*]

1 Shandong Provincial Key Laboratory of Depositional Mineralization and Sedimentary Minerals, College of Earth Science and Engineering, Shandong University of Science and Technology, Qingdao 266590, China; 15650147656@163.com (J.W.); zhaoyanhong65@126.com (Y.Z.); wgzhen321@163.com (G.W.); z17806255037@163.com (X.Z.)

2 Laboratory for Marine Mineral Resources, Qingdao National Laboratory for Marine Science and Technology, Qingdao 266237, China

3 Department of Bioengineering, College of Chemical and Environmental Engineering, Shandong University of Science and Technology, Qingdao 266590, China; 15689435926@163.com (J.Z.); zhanghucheng980301@163.com (H.Z.)

4 School of Earth Sciences, University of Bristol, Bristol BS8 1RJ, UK; glmet@bristol.ac.uk

5 Cabot Institute, University of Bristol, Cantock's Close, Bristol BS8 1UJ, UK

6 Qingdao West Coast District No. 1 Senior High School, Qingdao 266555, China; yinjunxiao_yizhong@163.com

* Correspondence: hanzuozhen65@126.com (Z.H.); zhsdust@126.com (H.Z.); 15954804511@163.com (H.Y.); Tel.: +86-532-86-057-286 (Z.H.); +86-532-86-057-813 (H.Z.); +86-532-86-057-625 (H.Y.)

Received: 30 December 2018; Accepted: 4 April 2019; Published: 6 April 2019

Abstract: Biomineralization induced by microorganisms has become a hot spot in the field of carbonate sedimentology; however, the mechanisms involved still need to be explored. In this study, the bacterium *Bacillus subtilis* J2 (GenBank MG575432) was used to induce the precipitation of calcium carbonate minerals at Mg/Ca molar ratios of 0, 3, 6, 9, and 12. *Bacillus subtilis* J2 bacteria released ammonia to increase pH, but the ammonia released only made the pH increase to 8.25. Carbonic anhydrase was also produced to catalyze the hydration of carbon dioxide, and this process released carbonate and bicarbonate ions that not only increased pH but also elevated carbonate supersaturation. The biominerals formed at a Mg/Ca molar ratio of 0 were spherulitic, elongated, dumbbell-shaped, and irregularly rhombohedral calcite; at a Mg/Ca molar ratio of 3, the biominerals were calcite and aragonite, the weight ratio of calcite decreased from 26.7% to 15.6%, and that of aragonite increased from 73.3% to 84.4% with increasing incubation time. At higher Mg/Ca molar ratios, the biominerals were aragonite, and the crystallinity and thermal stability of aragonite decreased with increasing Mg/Ca molar ratios. FTIR results showed that many organic functional groups were present on/within the biominerals, such as C–O–C, N–H, C=O, O–H, and C–H. HRTEM-SAED examination of the ultra-thin slices of *B. subtilis* J2 bacteria showed that nano-sized minerals with poor crystal structure had grown or been adsorbed on the EPS coating. The EPS of the *B. subtilis* J2 strain contained abundant glutamic acid and aspartic acid, which could be deprotonated in an alkaline condition to adsorb Ca^{2+} and Mg^{2+} ions; this made EPS act as the nucleation sites. This study may provide some references for further understanding of the mechanism of biomineralization induced by microorganisms.

Keywords: *Bacillus subtilis*; biomineralization; nucleation site; Mg/Ca ratio; amino acid; crystallinity; thermal stability; organic functional group; carbonic anhydrase; ammonia

1. Introduction

Biomineralization refers to the process where the formation of certain kinds of inorganic minerals can be regulated by some organisms. The biggest difference between biomineralization and general mineralization lies in the participation of bio-macromolecular metabolism, cells, and organic matrix. The product of biomineralization, namely, biominerals, can be carbonate, phosphate, sulfate, sulfide, silicate, hydroxide or oxide, and involve different species of cations such as calcium, magnesium, iron, and/or manganese [1–15]. In the process of bacterially induced mineralization, microorganisms can release metabolic products to react with metal ions in the environment, and the process usually results in the subsequent precipitation of mineral crystals [16–21]. The precipitation of calcium carbonate ($CaCO_3$) induced by microbes is a common process in aquatic environments [22–27]. Calcite, aragonite, and vaterite are the major crystalline polymorphs of $CaCO_3$ induced by bacteria [28]. Microbial mineralization processes and their products can be used in many ways. For example, recent literature has shown that the precipitation of calcite minerals by microbes within the pores of a rock can quickly reduce its permeability to water [29]. *Micrococcus* sp. and *Bacillus subtilis* were inoculated into some limestone samples and the consequence was that water absorption decreased by 60% [30]. Besides restricting the water penetration, the product of biomineralization induced by bacteria can also limit the exchange between the pores of the limestone and the atmosphere to protect the rock [31]. Based on the discovery of biomineralization, researchers have begun to develop new cementing materials. Biomineralization can also be used in the treatment of environmental pollution such as the removal or fixing of heavy metals [32,33] and the depletion of carbon dioxide [34–38].

Carbonate mineralization induced by microorganisms has been investigated in many studies [39–53]. However, there are still a large number of questions to be answered. For example, pH values in certain environments have been shown to increase in the presence of bacteria, and most scientists have believed that this is due to the ammonia released by bacteria [54]; however, other scientists have found that the quantity of ammonia released by bacteria is not enough to increase pH beyond 9.0 [51]. Thus, the question is: what is causing the pH to rise? This is a question worthy of further enquiry. The scientific problem of nucleation sites is also a focus for many researchers. It has been reported that nucleation sites for carbonate precipitation are present on cell walls, since ion exchange can take place through the cell membrane [55]. However, it has been shown that extracellular polymeric substances (EPS) are the nucleation sites for carbonate precipitation, rather than the cell wall [56]. Thus, the matter of nucleation sites and nucleation mechanisms also need to be further explored. At the same time, the thermal stability of biominerals has rarely been examined. Therefore, in view of these issues, the mechanisms of biomineralization induced by bacteria and the characteristics of biominerals precipitated need to be studied further.

In this study, the *B. subtilis* J2 strain was identified by the sequence of 16S rDNA, and then used to precipitate the calcium carbonate biominerals at Mg/Ca molar ratios of 0 (no Mg), 3, 6, 9, and 12. To further explore the mechanism of biomineralization, the variations of ammonia and carbonic anhydrase (CA) and the concentrations of the carbonate, bicarbonate, and ammonium ions were all investigated. The biominerals obtained were studied by X-ray diffraction (XRD), scanning electron microscopy (SEM)-energy dispersive spectrometer (EDS), Fourier transform infrared spectroscopy (FTIR), thermogravimetry (TG), differential thermogravimetry (DTG), and differential scanning calorimetry (DSC). To further determine the nucleation sites, ultrathin slices of *B. subtilis* J2 bacteria were prepared and analyzed by high-resolution transmission electron microscopy (HRTEM), selected area electron diffraction (SAED), and scanning transmission electron microscopy (STEM). To explore the mechanism of nucleation on the EPS, the EPS of *B. subtilis* J2 bacteria were extracted and the amino acids of the EPS were also analyzed. This study may shed light on the mechanism of biomineralization and contribute to the further understanding of the important role microorganisms play in nature.

2. Materials and Methods

2.1. Bacterial Strain and Culture Medium

Bacillus subtilis J2 bacteria were preserved at −20 °C in the laboratory of Zuozhen Han. The liquid culture medium used to incubate *B. subtilis* bacteria had the following components ($g \cdot L^{-1}$, deionized water): beef extract 3.0, tryptone 10.0, and NaCl 5.0. The solid culture medium was prepared by adding 20.0 g of agar powder into 1 L of the liquid culture medium. The pH values of the liquid and solid culture mediums were adjusted to 7.0.

2.2. 16S rDNA Identification of B. Subtilis J2 Bacteria

The total DNA of *B. subtilis* bacterium was extracted by the modified cetyltrimethylammonium bromide (CTAB) method [57] and the universal primers used were according to the description of the article [58]. Its 16S rDNA was sequenced by Shanghai Sangon Biotech Co., Ltd (Shanghai, China). The fragment assembly was performed by DNAMAN 8.0 software (Version 8.0, Lynnon Biosoft, Vaudreuil, QC, Canada) to obtain the complete 16S rDNA sequence. The basic local alignment search tool (BLAST) was used to compare the sequence homology between the 16S rDNA sequence of J2 bacteria and those of other bacteria in the GenBank. The phylogenetic tree of J2 bacteria was constructed using MEGA 7.0 software (Version 7.0, The Pennsylvania State University, Philadelphia, PA, USA) via the neighbor-joining method.

2.3. Morphology of Colony and Cell, Gram Staining, and Ammonia Test of B. Subtilis Bacteria

The morphology of *B. subtilis* J2 colony was observed with the naked eye and photos were taken using a camera (Canon, EOS 750D, Tokyo, Japan). The morphology of single *B. subtilis* J2 bacterium was analyzed by a scanning electron microscope (SEM, FEI Quanta 200, FEI, Hillsboro, OR, USA). The detailed steps for SEM and the Gram staining experiments were performed according to the published reference of Han et al. [40]. The stained *B. subtilis* J2 bacteria were analyzed by a microscope (Axio Lab A1, Carl Zeiss MicroImaging GmbH, Gottingen, Germany). An ammonia test of the *B. subtilis* bacteria was performed following the procedure of Zhuang et al. [51].

2.4. Preparation of the Bacterial Seed of B. subtilis J2

The bacterial seed was prepared according to the method reported by Zhuang et al. [51]. The concentration of *B. subtilis* bacteria in the bacterial seed was measured by a spectrophotometer (722s, Shanghai Precision and Scientific Instrument Corporation, Shanghai, China) at a wavelength of 600 nm. When the OD_{600} reached 1.0 or so, the preparation of the bacterial seed containing *B. subtilis* bacteria to be used in experiments was complete.

2.5. Growth Curve and pH Changes of B. subtilis Bacteria

The bacterial seed of the *B. subtilis* strain was inoculated into 300 mL of the sterile liquid culture medium in a 500-mL conical flask at an inoculation ratio of 1% and this was set as the experimental group. A control group was inoculated with sterilized distilled water (*v*:*v* = 1:100). All the experiments were performed in triplicate. All the cultures were placed in an oscillation incubator with a speed of 130 rpm at 37 °C. The concentration of the sample was measured by the spectrophotometer at a wavelength of 600 nm and pH values were measured by a pH meter (PHS-3, Jiangsu Jiangfen Instrument and Equipment Company, Jiangsu, China). The pH values at 195 h in the experimental and control group were analyzed by SPSS 21.0 software (Version 21.0, International Business Machines Corporation, Armonk, NY, USA).

2.6. Concentration of Ammonium Ions and pH Values

The concentration of ammonium ion in the liquid culture medium was measured following the procedure of Zhuang et al. [51]. According to the concentration of ammonium ions, pH values could be calculated by the method of Zhuang et al. [51]. The significant difference in pH values between that caused by ammonia and the experimental group was analyzed by SPSS 21 software.

2.7. CA Activity, Concentration of CO_3^{2-} and HCO_3^- Ion, and pH Values

In this study, CA activity (U/L) was defined as the amount of enzyme required to release 1 μmol of p-nitrophenol per min and 1 L. Carbonic anhydrase activity and the concentrations of CO_3^{2-} and HCO_3^- ions were measured according to the procedure of Zhuang et al. [51]. In order to determine what level the pH value could reach by the released CO_3^{2-} and HCO_3^- ions, the Na_2CO_3 + $NaHCO_3$ solution was prepared according to the concentration of CO_3^{2-} and HCO_3^- ions. The pH value of the Na_2CO_3 + $NaHCO_3$ solution was measured by a pH meter. All the experiments were performed in triplicate.

2.8. Minerals Induced by B. subtilis J2 at Different Mg/Ca Ratios

The Ca^{2+} concentration was 0.01 mol/L in the liquid culture medium, and the Mg/Ca molar ratio was adjusted to 0, 3, 6, 9, and 12 using anhydrous magnesium sulfate. After being sterilized by an autoclave (LDZX-50KBS, Shanghai Shen'an Medical Device Factory, Shanghai, China) at 110 °C for 25 min, the liquid culture medium was cooled to room temperature. Then, the solutions of Na_2CO_3 (2 mol·L^{-1}) and $NaHCO_3$ (1 mol·L^{-1}) were prepared and sterilized by a filter containing a 0.22 μm-pore-sized membrane. Three milliliters of Na_2CO_3 (2 mol·L^{-1}) and 6 mL of $NaHCO_3$ (1 mol·L^{-1}) filtrate were added to 150 mL of the sterilized liquid culture medium with a syringe. At last, the pH values were all adjusted to 7.0. At this time, the culture medium used to induce the precipitates was prepared. The bacterial seed (OD_{600} = 1.0) was inoculated into the liquid culture medium at a 1% inoculation ratio and this was set as the experimental group. The control group A was inoculated with the same volume of sterilized deionized water as that of the bacterial seed. The control group B was also set, and its composition was the same as control group A, except that its pH was adjusted to 9.22, which was the same as that of the experimental group at 195 h in the pH change curve. There were 3 parallel samples at each value of Mg/Ca ratio in the experimental and control groups.

2.9. Characterization of the Extracellular Mineral Precipitates

After 14 and 24 days of incubation, the mineral precipitates were analyzed by XRD (D/Max-RC, Rigaku Co., Tokyo, Japan), with a scanning angle from 10°–80°, a step size of 0.02, and a count time of 8°·min^{-1} [59–68]. The XRD data were analyzed by the Jade 6.5 software (Version 6.5, Materials Data Ltd., Livermore, CA, USA). The minerals in the control group B at Mg/Ca molar ratio of 0 were also analyzed according to the above steps.

The micromorphology, sizes, and elemental composition of the mineral precipitates cultured for 14 days were further analyzed by SEM (Hitachi S-4800, Hitachi, Tokyo, Japan) [69–76] and EDS (Apollo XLT SDD, EDAX, New York, NY, USA) after the mineral precipitates were coated with platinum (Pt) powder. The minerals in the control group B at Mg/Ca molar ratio of 0 were also analyzed according to the same steps.

The organic functional groups on/within the minerals were analyzed by FTIR (Nicolet 380, Thermo Fisher Scientific Inc., Waltham, MA, USA) [77,78] using the potassium bromide method in a scanning range of 400–4000 cm^{-1} with a resolution of 4 cm^{-1}.

The minerals were ground in an agate mortar, sifted through a 200-mesh sieve, and the powder was analyzed using the thermal analyzer (TGA/DSC1/1600LF, METTLER TOLEDO Co., Schwerzenbach, Switzerland) from 100 °C to 900 °C at a heating rate of 15 °C·min^{-1} with pure nitrogen as a protective

gas to prevent oxidation. The mass loss, peak temperature, and enthalpy change (ΔH) were described by the TG, DTG, and DSC [52,79–89].

2.10. Amino Acid Composition of EPS

Extracellular polymeric substances were extracted according to the modified heat treatment method [51]. The EPS powder was sent to Jiangsu Coastal Chemical Analysis and Technological Service Ltd. (Yancheng, China). Amino acid components in the EPS were analyzed by an amino acid analyzer (Hitachi L-8900, Tokyo, Japan).

2.11. Analyses of Intracellular Biomineralization

Ultra-thin slices of *B. subtilis* bacteria cultured at different Mg/Ca ratios and in the liquid culture medium without any Mg^{2+} and Ca^{2+} ions were prepared according to the literature [40]. The ultra-thin slices of *B. subtilis* bacteria were analyzed by HRTEM (H-7650, Hitachi, Tokyo, Japan) [90], SAED, and STEM (Tecnai G^2 F20, FEI, Hillsboro, OR, USA).

3. Results

3.1. 16S rDNA Identification of J2 Bacteria

The 16S rDNA of the J2 bacterium was 1486 bp in length and this was uploaded to the GenBank. The accession number given by GenBank was MG575432. The 16S rDNA of the J2 strain shares 100% homology with a large number of *B. subtilis* strains. The phylogenetic tree shown in Figure 1, based on the 16S rDNA sequence, proves that the J2 strain is related to a *B. subtilis* species, which has the closest sequence similarity.

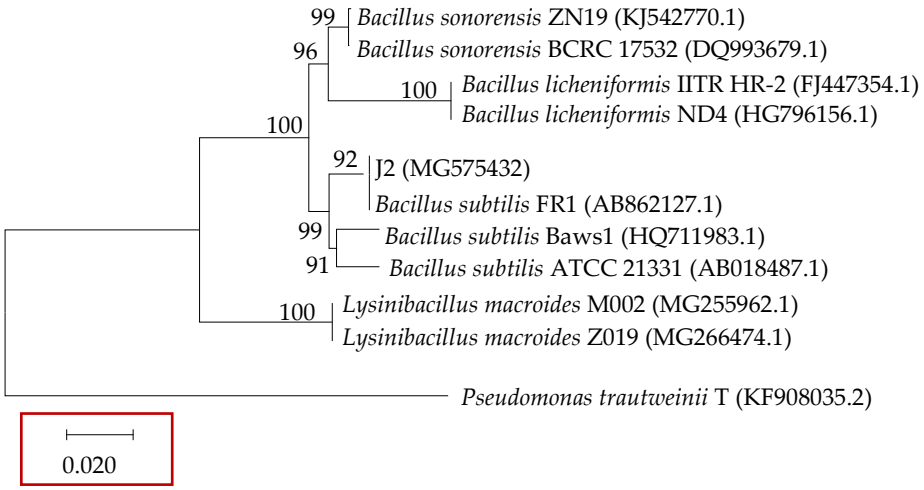

Figure 1. Phylogenetic tree of *B. subtilis* J2 bacterium constructed with neighbor-joining method.

3.2. Characterization of B. subtilis J2 Bacteria

3.2.1. Morphology of Colony and Cell, Gram Staining, and Ammonia Test of *B. subtilis* J2 Bacteria

Figure 2a shows the morphology of single colonies of *B. subtilis* J2 bacteria incubated for 5 days. The single colonies with neat and smooth edges are milky white and dome-shaped. The SEM image shown in Figure 2b reveals that the *B. subtilis* J2 bacterium is about 1.8 μm in length and 0.8 μm in width, and EPS, similar to a thin film, loosely wrap the cell. The result of Gram staining shown in Figure 2c is positive, indicating that *B. subtilis* J2 bacteria are Gram-positive. An ammonia test of *B.*

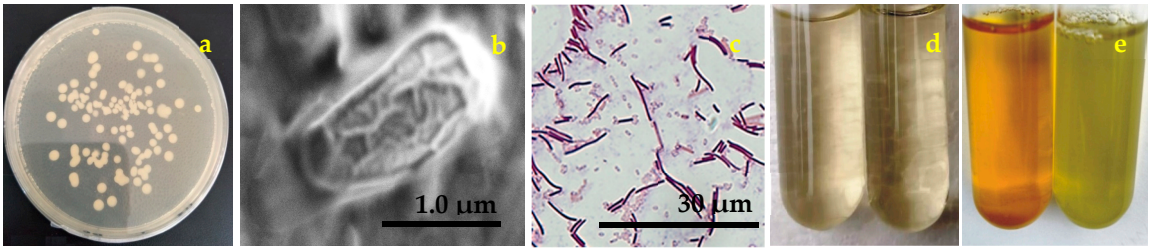

Figure 2. Characterization of *Bacillus subtilis* J2 bacteria. (**a**) A single colony on the solid plate; (**b**) the morphology in SEM view; (**c**) the Gram staining in a biological microscope view; (**d**) the sample before adding the Nessler's reagent; (**e**) the sample after adding the Nessler's reagent. In Figure 2d,e, the left is the experimental group inoculated with bacteria and the right is the control group without bacteria.

B. subtilis J2 bacteria were performed and the result is shown in Figure 2d,e. It can be seen there that the liquid in the experimental group (left tube in Figure 2d) is turbid due to the presence of *B. subtilis* J2 bacteria and the control group (right tube in Figure 2d) is transparent before adding the Nessler's reagent. After adding the Nessler's reagent, there was a great change in the color. The experimental group showed a dark-brown color (Figure 2e, left); the control group presented a yellow color (Figure 2e, right), the color of Nessler's reagent. Thus, the result of the ammonia test of *B. subtilis* J2 bacteria was positive, meaning that *B. subtilis* J2 bacteria were able to release ammonia.

3.2.2. The Growth Curve of *B. subtilis* J2 and pH Variation in the Liquid Culture Medium

As shown in Figure 3a, the growth process of *B. subtilis* J2 bacteria can be divided into four main phases: the delay/adaption phase, the logarithmic growth phase, the stationary phase, and the decline phase. The time range of the adaption phase was 0–2 h; in the meantime, there was almost no increase in the concentration of the *B. subtilis* J2 bacterial cells. The exponential growth period was over a time range of 2–38 h, during which there was a sharp increase in the *B. subtilis* J2 bacterial concentration. The third stage was a stable phase in a time range of 38–46 h; the cell concentration of *B. subtilis* J2 bacteria was almost unchanged. The last stage was a decline phase from 46–195 h; the cell concentration sharply decreased from 1.2×10^9 to 0.16×10^9 cfu/mL. A large consumption of nutrients led to a shortage of carbon and nitrogen in the liquid culture medium, which limited the proliferation of bacteria and resulted in a great decrease in the cell concentration [43]. Figure 3a also showed that there was a significant difference in pH values between the control group and the experimental group ($p < 0.01$). As shown in Figure 3a, the pH in the experimental group can increase to 9.22 with an extension of the incubation time. However, the pH value in the control group was almost unchanged and kept at 7.0 or so. It can be concluded that *B. subtilis* J2 bacteria played an important role in the pH increase, and that the highly alkaline environment created by *B. subtilis* J2 was beneficial to the precipitation of carbonate minerals.

3.2.3. Ammonium Concentration and pH Value based on the Concentration of Ammonium

B. subtilis J2 bacteria were able to release ammonia, and this was confirmed by the ammonia test. The next question considered was how much ammonia *B. subtilis* J2 bacteria could release and whether the released ammonia could satisfy the requirement of a pH increase up to 9.22. Thus, the concentration of ammonium was measured, and pH values based on the concentration of ammonium were also calculated. It can be seen from Figure 3b that the concentration of ammonium increased sharply before 38 h and increased slowly after 38 h; this indicates that the quantity of ammonia released by *B. subtilis* strain decreased after 38 h. In order to determine how high the pH value could reach under the influence of ammonia released by the *B. subtilis* strain, pH values were calculated according to the concentrations of ammonium, and these are shown in Figure 3b. The pH value caused by the ammonia released only reaches about 8.25 and then keeps constant at 8.25 at 90 h, significantly much lower

than that in the experimental group (pH = 9.22, $p < 0.01$). This shows that there must be other factors causing the increase in pH in the experimental group besides ammonia.

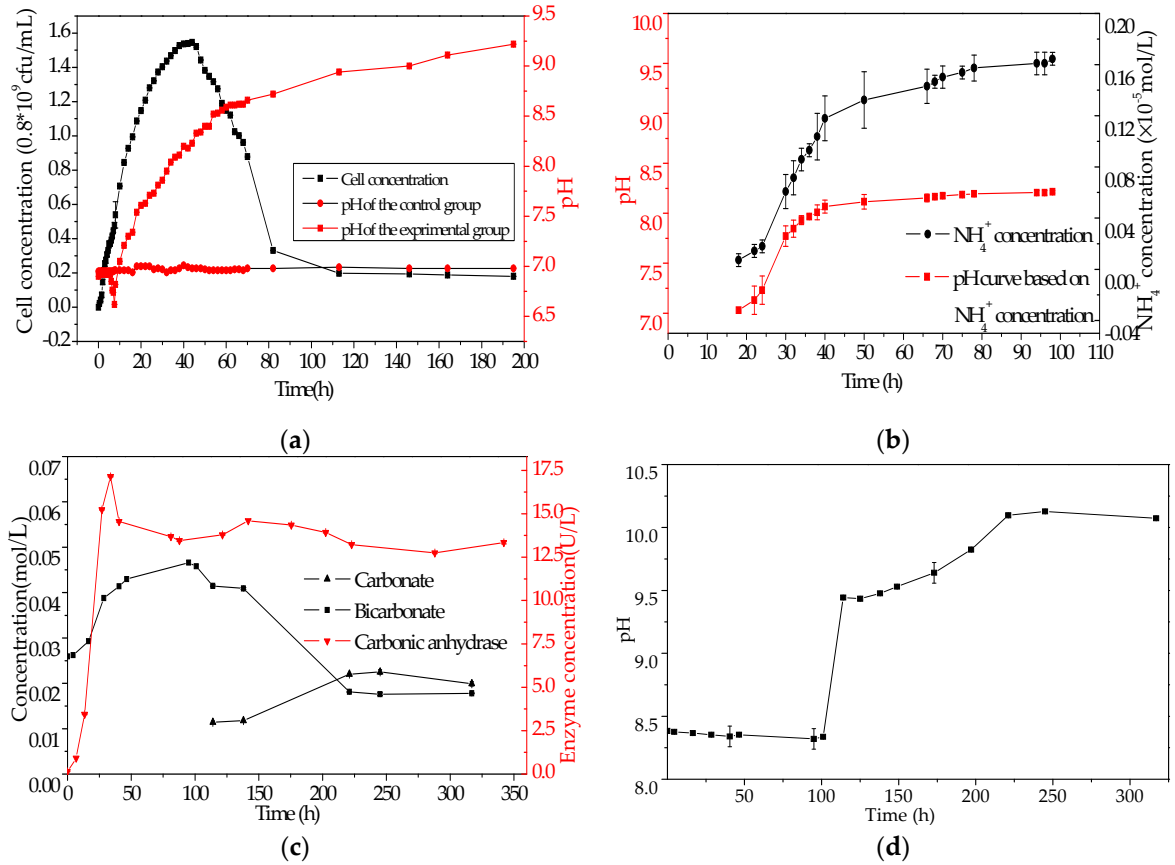

Figure 3. Physiological and biochemical characteristics of the *B. subtilis* J2 strain. (**a**) Growth curve and pH curve; (**b**) the concentration of ammonium and pH curve based on the concentration of ammonium; (**c**) concentrations of CA and bicarbonate and carbonate ions; (**d**) pH curve based on the concentration of bicarbonate and carbonate ions.

3.2.4. CA Activity and the Concentration of CO_3^{2-} and HCO_3^- Ions

The CA concentration was calculated according to the following standard Equation (1):

$$y = 9.0317x + 0.0349 \ (R^2 = 0.9974) \quad (1)$$

The CA concentration sharply increased from 0 to 17.14 U/L or so (0–15 h), and then decreased slightly and kept at 14.3 U/L (Figure 3c). The concentration of HCO_3^- ions increased from 0.026 to 0.048 mol/L in the time range 0–89 h, and then decreased from 89 h to 210 h, and finally kept almost constant at 0.0181 mol/L or so after 210 h (Figure 3c). Before 114 h, the concentration of CO_3^{2-} ions was too little to be measured. From 114 h to 210 h, CO_3^{2-} ions were rapidly produced and the concentration increased to 0.022 mol/L; from 210 h, the concentration of CO_3^{2-} ions was almost constant (Figure 3c). According to the concentration of HCO_3^- and CO_3^{2-} ions, the sodium bicarbonate and sodium carbonate solution was prepared, and their pH values were also measured. It can be seen from Figure 3d that the pH based on the sodium bicarbonate and sodium carbonate solution increased from 8.35 to 9.80 in the time range 0–200 h. This indicates that CA catalyzed the carbon dioxide hydration to release a large number of HCO_3^- and CO_3^{2-} ions, leading to a further increase in pH. Thus, the pH in the experimental group reaching 9.22 was mainly due to the effect of the CA combined with ammonia, because the ammonia released by the *B. subtilis* strain only increased the pH to 8.25.

3.3. Characterization of the Mineral Precipitates

3.3.1. Mineral Phases and Crystal Structures

In this study, no precipitates were observed by the naked eye in the control group A at different Mg/Ca ratios of 0, 3, 6, 9, and 12 (Supplementary Materials, Figure S1a), probably due to the fact that the pH almost kept constant at 7.0. Maybe it needed a longer time to precipitate the minerals. In the control group B, the mineral precipitates were present at a Mg/Ca ratio of 0, and there were colloidal substances at other Mg/Ca ratios (Supplementary Materials, Figure S1b$_1$,b$_2$), but no mineral precipitates. In order to better understand the mineral types in the control group B at the Mg/Ca molar ratio of 0, the precipitates were analyzed by XRD. According to the XRD results (Supplementary Materials, Figure S2), the mineral was calcite. The colloidal substances at other Mg/Ca ratios could not be obtained and were abandoned. Thus, there was a great difference between the control groups and the experimental group because the minerals in the experimental group could be observed by the naked eye, while in the control group could not, except for the control group B at the Mg/Ca molar ratio of 0. Therefore, the following experiments were mainly conducted on the minerals in the experimental group, and the control groups will be studied in the future.

To determine the mineral phases present, the minerals cultured for 14 days and 24 days were analyzed by XRD; results are shown in Figure 4a,b, respectively. Figure 4a for the 14 days' experiments shows that the diffraction angles (2θ) of the minerals at a Mg/Ca molar ratio of 0 were 23.1°, 29.4°, 31.4°, 36.0°, 39.4°, 43.2°, and 47.1°, corresponding to the (*hkl*) indices (012), (104), (006), (110), (113), (202), and (024), respectively, of the mineral calcite. The corresponding peak full-width at half maximum (FWHM, unit: degree) (104) was found to be 0.246. At a Mg/Ca molar ratio of 3 (Figure 4a), the diffraction angles (2θ) were 19.0°, 21.1°, 22.3°, 26.2°, 27.2°, 31.1°, 32.7°, 33.1°, 36.1°, and 36.2°, corresponding to the (*hkl*) indices (011), (110), (020), (111), (021), (002), (121), (012), (102), and (200), respectively, of the mineral aragonite. According to the diffraction angles (2θ) 29.4°, 36.0°, 43.2°, corresponding to the (*hkl*) indices (104), (110), and (202), calcite was also present in Figure 4a at a Mg/Ca molar ratio of 3, besides aragonite. The weight ratio of aragonite was 73.3% and that of calcite was 26.7% using the Jade 6.5 software. At Mg/Ca molar ratios of 6, 9, and 12, the only mineral present was aragonite. Furthermore, the FWHM of the corresponding peak (111) was found to be 0.177, 0.222, and 0.224 at the Mg/Ca molar ratios of 3, 6, and 12, respectively; this indicates that the crystallinity of aragonite decreased with an increase in the concentration of magnesium. Figure 4b for the 24 days' experiments shows that the mineral was still calcite at a Mg/Ca molar ratio of 0, and the FWHM (104) was 0.163, much lower than that of calcite cultivated for 14 days (0.246); this indicates that the crystallinity of calcite increased with the longer incubation time. At a Mg/Ca molar ratio of 3, with both calcite and aragonite, the weight ratio of aragonite was 84.4% and that of calcite was 15.6% using the Jade 6.5 software, indicating that the weight ratio of aragonite increased with the longer incubation time. As shown in Figure 4b, with only aragonite at Mg/Ca molar ratios of 6, 9, and 12, the FWHM of the corresponding peak (111) increased from 0.153 to 0.176, indicating that the crystallinity of aragonite decreased with an increase in the concentration of magnesium; this was consistent with the result of the aragonite cultivated for 14 days. Moreover, the FWHM of the corresponding peak (111) decreased with the incubation time at Mg/Ca molar ratios of 3 and 12, indicating that the crystallinity of aragonite increased with the longer incubation time.

3.3.2. Morphology and Elemental Composition of the Minerals

The calcite precipitates in the control group B at a Mg/Ca molar ratio of 0 were also analyzed by SEM and EDS. They were in a shape of elongate (Supplementary Materials, Figure S3a), regular rhombohedron (Figure S3b), and irregular rhombohedrons (Supplementary Materials, Figure S3c,d). The elemental composition in the three kinds of calcites was Ca, C, and O (Supplementary Materials, Figure S3e–g). The morphology of calcite in the control group B was significantly different from that in the experimental group. The morphology of calcite in the experimental group was more diverse.

Figure 5a$_{1–4}$ show that there are spherulitic, elongate, dumbbell-shaped, and irregularly rhombohedral calcite at a Mg/Ca molar ratio of 0, and the elemental composition of the spherulitic mineral marked with a red square shown in Figure 5a$_1$ includes Ca, C, O, Al, and P (Figure 5a$_5$). The Ca, C, and O come from calcite; the Al originates from the aluminum sample mount. The presence of P suggests that there may be a close relationship between the bacteria and the minerals precipitated. In the presence of Mg^{2+}, significant changes took place in the mineral morphology; this is likely due to the fact that the mineral calcite was replaced by the new mineral phase aragonite when the Mg/Ca molar ratio changed from 0 to 3. It can be seen from Figure 5b$_{1–4}$ that the minerals at a Mg/Ca molar ratio of 3 do not have regular geometric features any more, but conversely, have become irregular; some holes and depressions can be clearly observed which are likely marks left by the shedding of microbial cells (Figure 5b$_4$). These holes further indicate that *B. subtilis* J2 bacteria played an important role in the growth process of the minerals. Figure 5b$_5$ shows the elemental composition of the area marked by a red square in Figure 5b$_4$ and the elements include Ca, C, O, Al, and P. No Mg was present, maybe because the concentration of Mg^{2+} in the liquid culture medium was too low or the quantity of Mg adsorbed on/within the mineral was below the detection limit. The spherulitic minerals occurred again, as well as irregular minerals but with an increase in Mg^{2+} concentration (Figure 5c$_1$). The morphology and size were significantly different from those of the spherulitic calcite shown in Figure 5a$_1$, which was up to 10 μm in diameter and composed of many polygonal crystals. The spherulitic mineral shown in Figure 5c$_1$ was about 30–40 μm in diameter, with a smooth surface. There was a bacterium on the surface of some minerals, shown in the center of Figure 5c$_2$, and the mineral was composed of irregular minute micron-size crystals. Figure 5c$_3$ also shows a bacterium on the surface of the mineral and this bacterium was significantly different from the bacterium shown in Figure 5c$_2$. The bacterium was larger than that in Figure 5c$_2$, rod-shaped, and surrounded with nanometer-size minerals; the EPS of this bacterium acts as a glue to attach the bacterium to the mineral surface. While the bacterium in Figure 5c$_2$ was much smaller than that shown in Figure 5c$_3$, it could be that it was in a younger state or a spore. Figure 5c$_4$ shows that the mineral was composed of band-shaped crystal aggregates. The elements of the spherulitic mineral shown in Figure 5c$_1$ include Ca, C, O, Al, P, and Mg (Figure 5c$_5$). The Mg maybe originated from the culture medium or the Mg adsorbed on/within the mineral, further indicating that Mg^{2+} ions were involved in the growth of aragonite minerals. At a Mg/Ca molar ratio of 9, the dumbbell-shaped minerals developed into an elliptical mineral and the long axis of symmetry was over 50 μm (Figure 5d$_1$). Figure 5d$_2$ shows a mass of mineral shells with a length of about 1 μm, basically the size of a spore. There was a small hole growing on the end of a complete mineral shell; this could be a pathway to connect to the outside environment for the spores in the mineralized shells. There was also a mineral shell wrapping around the bacterium (Figure 5c$_3$), obviously larger than that of the spore shown in Figure 5d$_2$. Figure 5d$_3$ shows the micromorphology of some minerals. It can be seen that some granular particles growing into elongate minerals cover the surface of the mineral, similar to the morphology shown in Figure 5b$_3$,c$_4$. The elongate minerals were smaller, possibly due to the higher concentration of Mg^{2+} ions in the liquid culture medium. The elemental composition shown in Figure 5d$_5$ indicates that the mineral shell marked by a red square shown in Figure 5d$_2$ contained Ca, C, O, Al, P, and Mg. The mineral shell enveloping the bacterium or spore further indicates that the nucleation site of biomineralization induced by *B. subtilis* J2 was the EPS. Figure 5e$_1$,e$_2$ show that the mineral aggregates (Figure 5e$_2$) were composed of dumbbell-shaped minerals, which consist of a larger and a smaller spherical mineral (Figure 5e$_1$). The different sizes of spherical minerals in the dumbbell-shaped minerals suggest the growth rate of the larger spherical mineral was higher than that of the smaller spherical mineral. The reason for different growth rates needs to be explored further. Besides the mineral aggregates, there was also a fusiform mineral about 5 μm in length. The elements contained in the larger spherical mineral of the dumbbell-shaped mineral shown in Figure 5e$_1$ included Ca, C, O, Al, P, Mg, and Na (Figure 5e$_5$). Ca, C, and O elements come from the calcium carbonate minerals. The Al originates from the aluminum sample mount. The presence of P suggests that there may be a close relationship between the bacteria and the minerals precipitated. The Mg and Na

elements come from the liquid culture medium. No precipitates were obtained in the control group, indicating that aragonite could not be formed even at a higher Mg^{2+} concentration in the absence of *B. subtilis* J2 bacteria; this further indicates that the *B. subtilis* J2 bacteria played an important role in the formation of aragonite, in addition to the role of magnesium.

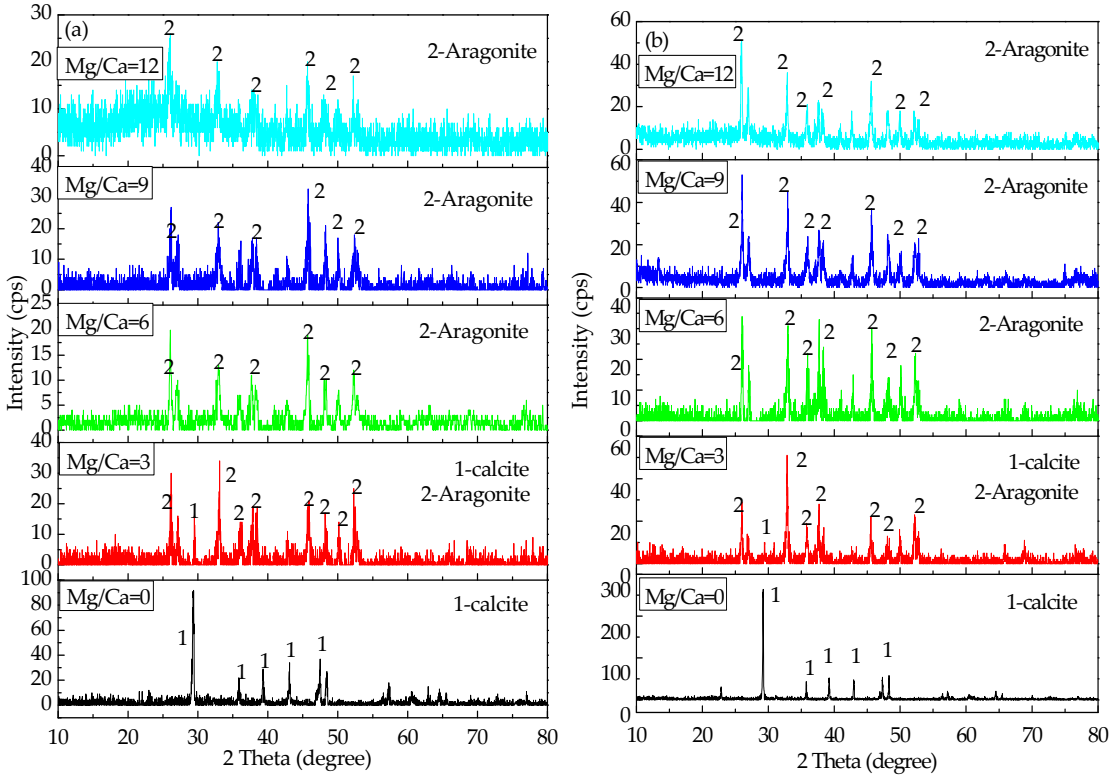

Figure 4. X-ray diffraction (XRD) analyses of the minerals cultured for 14 days (**a**) and 24 days (**b**).

3.3.3. FTIR Analyses of the Minerals

Figure 6 shows the characteristic peaks of calcite, aragonite, and organic functional groups. The characteristic peaks of aragonite were at 710 cm^{-1}, 856 cm^{-1}, 1082 cm^{-1}, and 1475 cm^{-1}, and those of calcite were 712 cm^{-1}, 875 cm^{-1}, 1421 cm^{-1}, and 2514 cm^{-1} [91]. The peaks at 712 cm^{-1}, 875 cm^{-1}, and 2514 cm^{-1} were the characteristic peaks of calcite (Figure 6a) and this indicates that the mineral at the Mg/Ca molar ratio of 0 was calcite. Figure 6b shows that the characteristic peaks were at 712 cm^{-1} and 874 cm^{-1} and this proves that the mineral was also calcite. There were also some other characteristic peaks in Figure 6b, such as 856 cm^{-1}, 1082 cm^{-1}, and 1488 cm^{-1} and these indicate the presence of aragonite. It can be seen from Figure 6c that the characteristic peaks were at 710 cm^{-1}, 856 cm^{-1}, 1082 cm^{-1}, and 1479 cm^{-1}; Figure 6d shows the characteristic peaks were at 710 cm^{-1}, 858 cm^{-1}, 1082 cm^{-1}, 1479 cm^{-1}; and Figure 6e shows the characteristic peaks were at 710 cm^{-1}, 856 cm^{-1}, and 1082 cm^{-1}. From the characteristic peaks shown in Figure 6c–e, the minerals were aragonite at the Mg/Ca molar ratios of 6, 9, and 12. The mineral phases obtained at each value of Mg/Ca molar ratio were consistent with the results of XRD. Figure 7f shows the vibrational bands of C–O–C (1072 cm^{-1}), N–H (1455 cm^{-1}), C=O (1798 cm^{-1}), O–H (2359 cm^{-1}), and C–H (2929 cm^{-1}) [40]. Figure 6g,h also show the same organic functional groups. Besides these, the vibrational band of C=O (1415 cm^{-1}) originating from the carboxyl group was also present (Figure 6g). These organic functional groups could have come from the culture medium or from *B. subtilis* J2 bacteria. The morphology of minerals can be affected by some particular organic functional groups [92]; e.g., the formation of the elongate calcite has been related to the C=O group [93]. As to what can affect the morphology of calcite and aragonite, further study is needed.

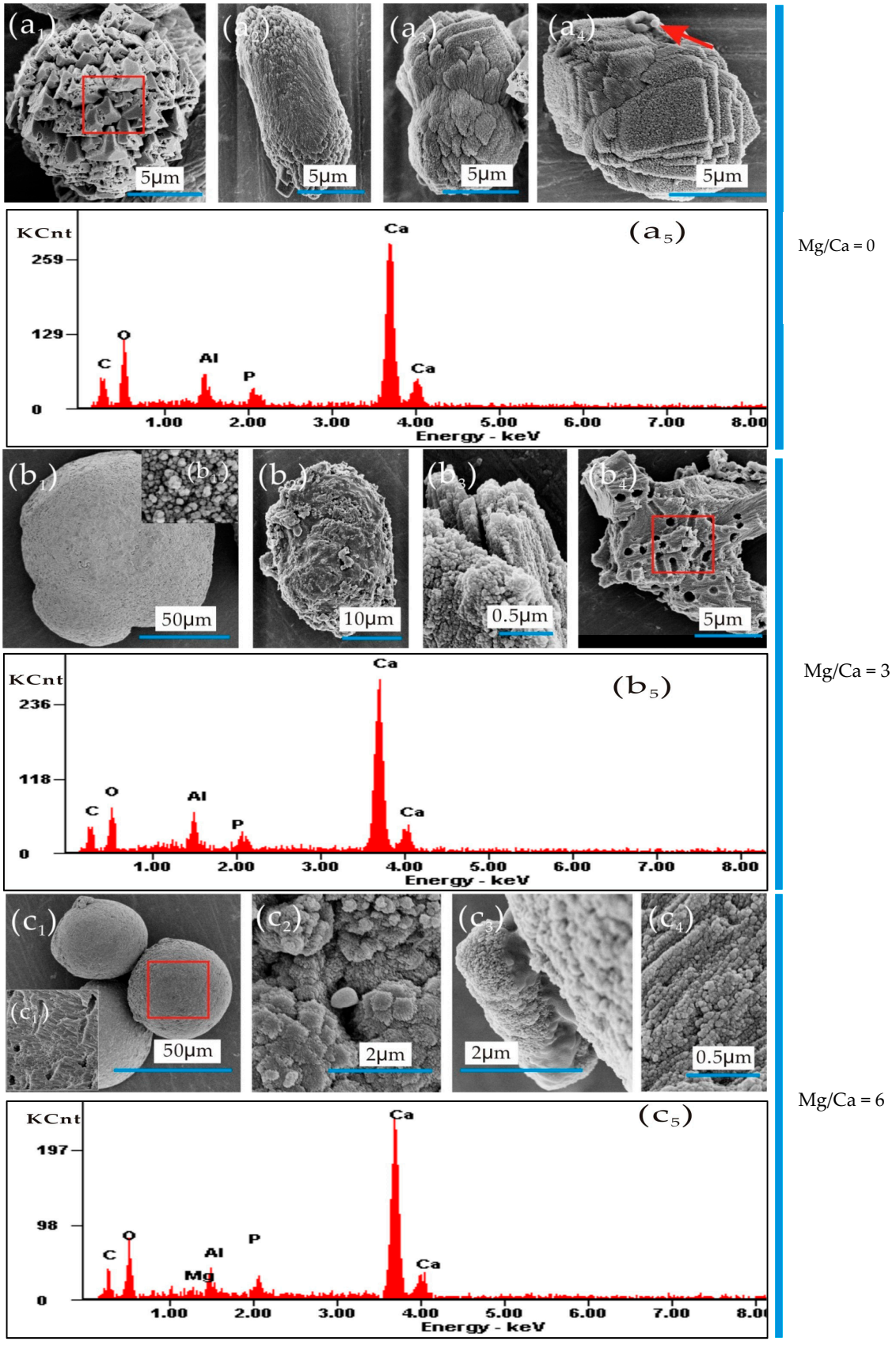

Figure 5. *Cont.*

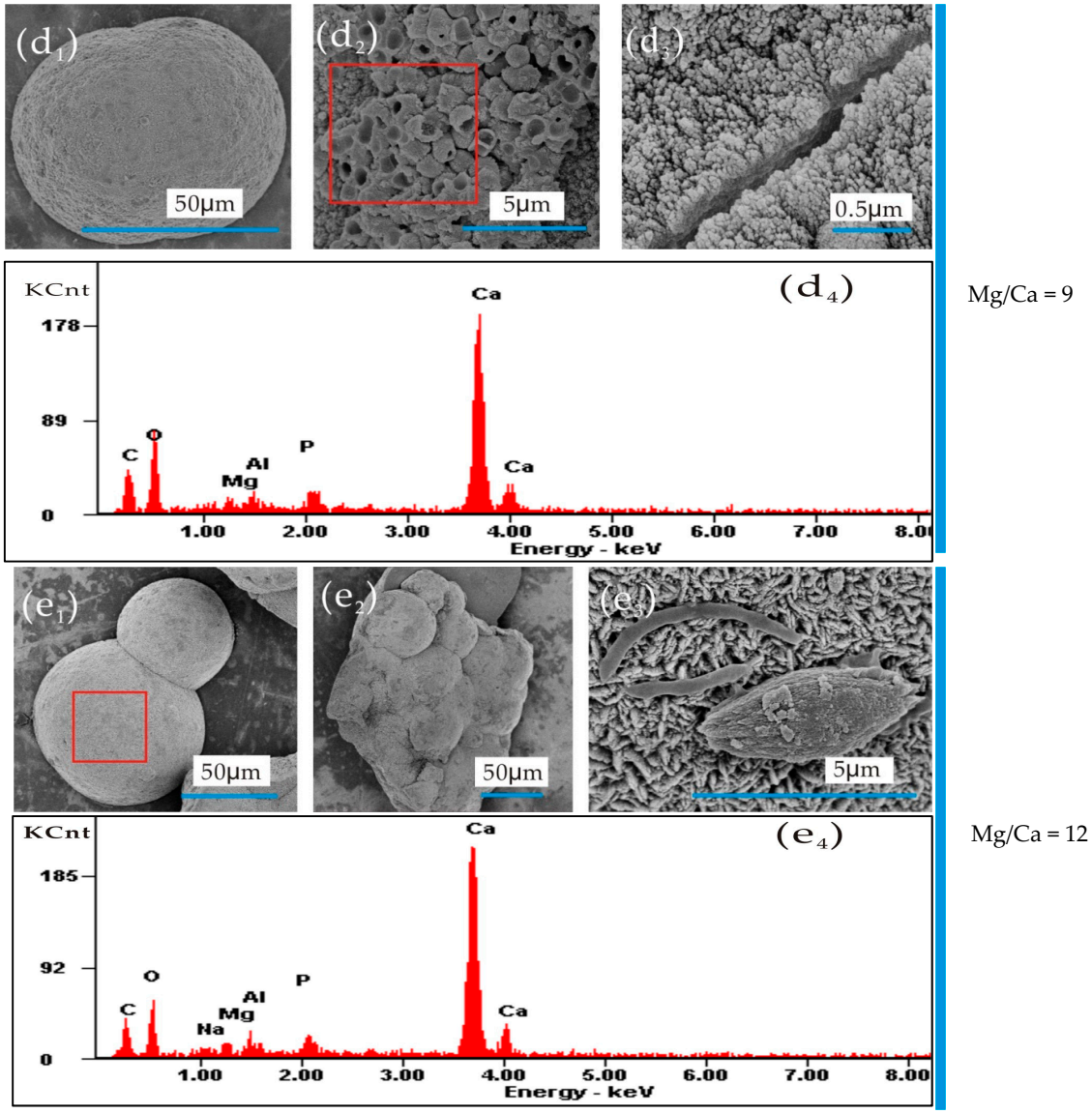

Figure 5. Scanning electron microscopy (SEM) and energy dispersive spectrometer (EDS) images of mineral precipitates cultured for 14 days.

3.3.4. TG, DTG, and DSC Analyses of the Minerals

The aragonites at the Mg/Ca molar ratios of 6, 9, and 12 were analyzed by TG, DTG, and DSC (Figure 7). Figure 7a shows that the final mass loss ratio of the aragonite at a Mg/Ca molar ratio of 12 was 47.41%, more than that of the aragonite at Mg/Ca molar ratios of 9 (47.33%) and 6 (47.02%), respectively, suggesting that the thermal stability of aragonite decreases with an increase in the Mg/Ca molar ratio of the fluid. Figure 7b shows the DTG results and the three curves almost overlap. To clearly observe the peaks of the three curves, a small part of these are enlarged and shown in Figure 7c. The results show that the peak temperatures of aragonite at Mg/Ca molar ratios of 6, 9, and 12 were 785.52, 782.51, and 779.86 °C, respectively; these figures indicate that the thermal stability of aragonite decreases with an increase in the concentration of Mg^{2+} in the fluid. Figure 7d shows the DSC results and it can be seen from Figure 7d that the peak temperatures of aragonite at Mg/Ca molar ratios of 6, 9, and 12 were 787.01 °C, 785.98 °C, and 780.86 °C, respectively; these values also indicate that the thermal stability of aragonite decreases with an increase in the Mg/Ca molar ratio. The heat absorbed during the thermal decomposition process can also be measured by the change in enthalpy (ΔH) [51]. ΔH means the heat absorbed per unit sample mass. It can be seen from Figure 7d that

the enthalpy ΔH of the aragonites calculated from the peak area at a heating rate of 15 °C·min^{-1} was 3124.51 J/g, 2693.50 J/g, and 2549.17 J/g, corresponding to the peak temperatures of 787.01 °C, 785.98 °C, and 780.86 °C, respectively. Thus, the thermal stability of aragonite decreases with an increase in the Mg/Ca molar ratio. From Figure 4a,b, the crystallinity of aragonite decreases with the increasing Mg/Ca molar ratio, consistent with the results of thermal stability.

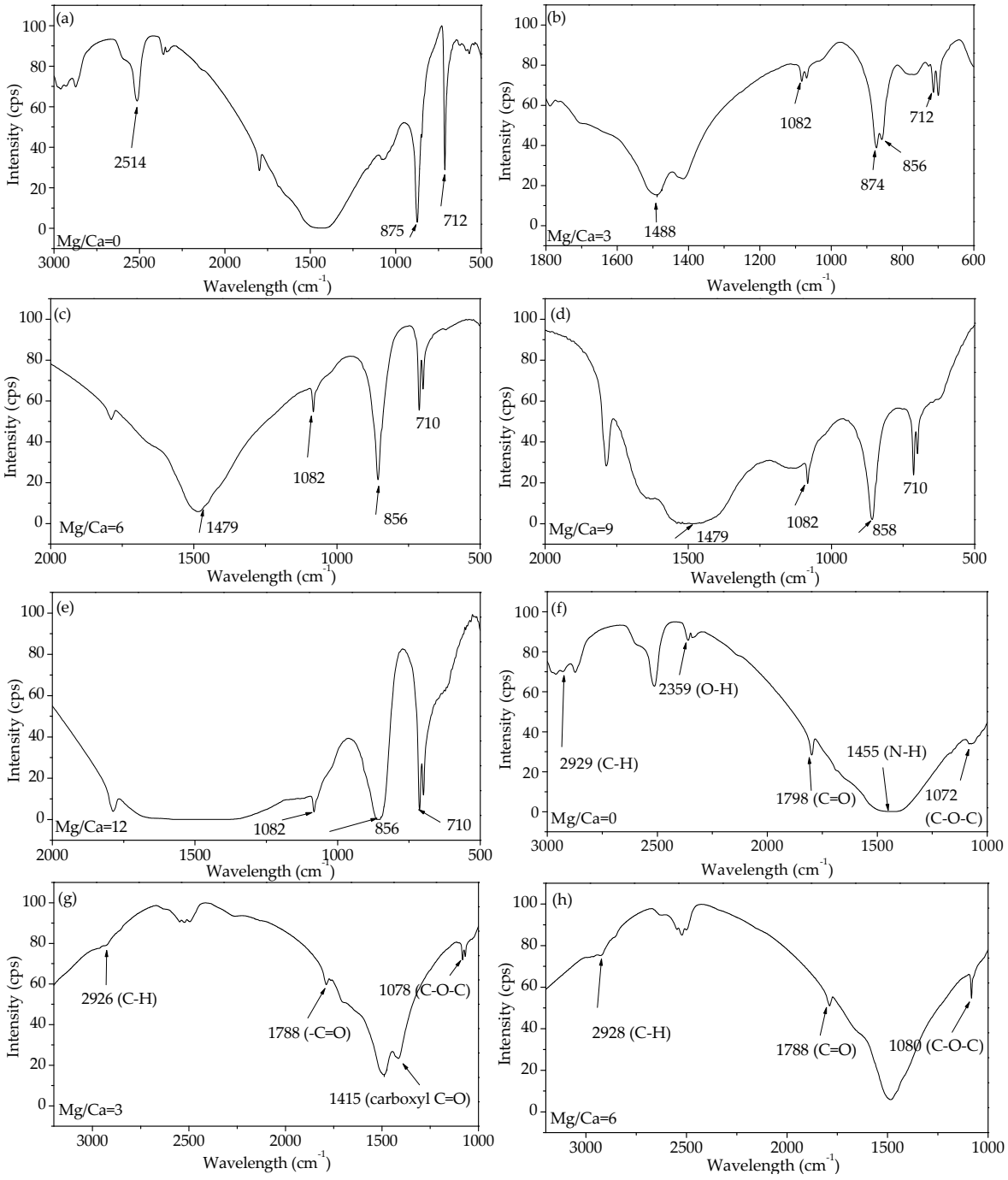

Figure 6. Fourier transform infrared spectroscopy analyses (FTIR) of the mineral precipitates cultured for 14 days.

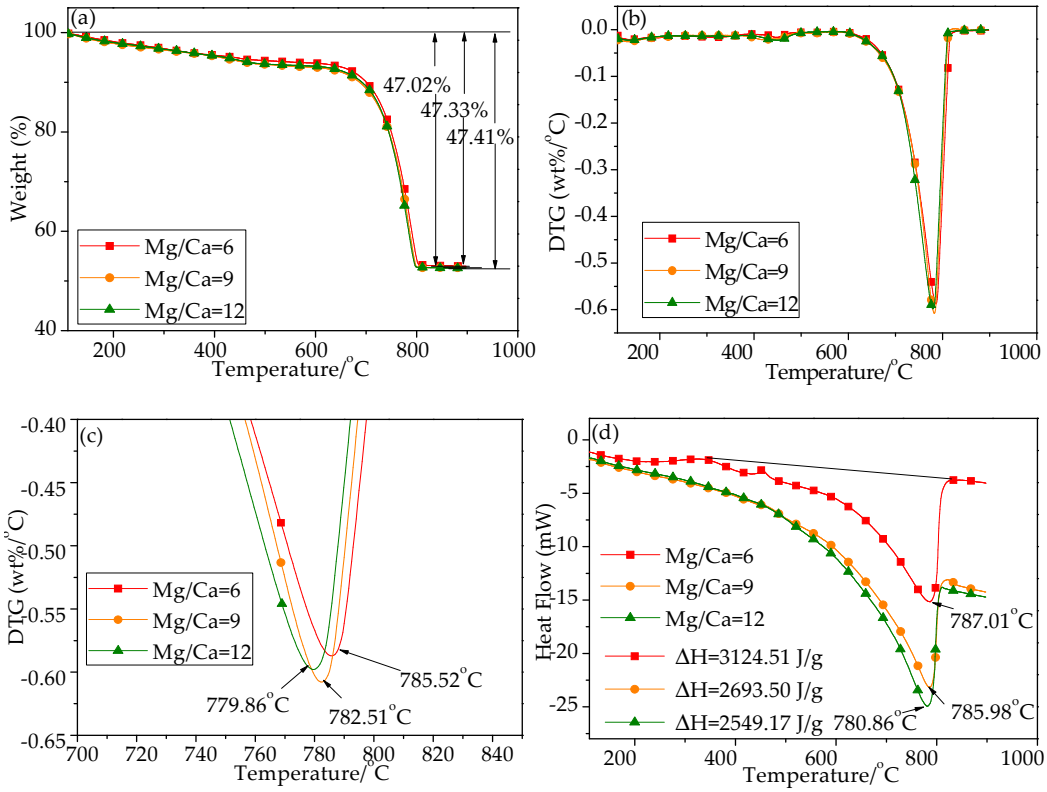

Figure 7. Thermogravimetry (TG) (**a**), differential thermogravimetry (DTG) (**b** and **c**), and differential scanning calorimetry (DSC) (**d**) analyses of the mineral precipitates cultured for 14 days.

3.4. HRTEM and SAED Analyses of Ultra-Thin Slices of B. subtilis J2 Bacteria

Ultra-thin slices of *B. subtilis* J2 bacteria with a thickness of 70 nm were prepared and analyzed by HRTEM and SAED. Figure 8a$_{1–4}$ show that there were some granular dark areas inside the cells incubated in the culture medium, only with beef extract, tryptone, and NaCl. The dark area shown in the HRTEM image indicates that the area was too thick to be penetrated by electrons. If the area contains abundant metal elements, it would also be dark. Thus, the dark areas shown in Figure 8a$_{1–4}$ may contain organic substances or metal elements, such as Na^+. It can be seen from Figure 8b$_1$ that there were also granular areas inside the cell. When the area marked by a red square (Figure 8b$_1$) is enlarged (Figure 8b$_2$), it appears to be an organelle. This area was also analyzed by SAED (Figure 8b$_3$) and the result shows that no mineral crystals were present inside the granular area because there no diffraction spots and rings were obtained (Figure 8b$_3$). There are many fibrous substances distributed on the cell surface or EPS (Figure 8b$_4$). At a Mg/Ca molar ratio of 6, dark dendritic areas appear inside the cells (Figure 8c$_{1,2}$). Figure 9c$_3$ shows that the dark granular areas are evenly distributed throughout the cell as well as on the cell surface/EPS, and the darkest area without any crystal structure (Figure 8c$_4$) is located directly in the center of the cell (Figure 8c$_3$). At a Mg/Ca molar ratio of 9, the dark dendritic areas still appear inside the cells (Figure 8d$_{1–3}$), but also do not show any crystal structure (Figure 9d$_4$). At a Mg/Ca molar ratio of 12, there was a collection of loose granular material (Figure 8e$_1$) with poor crystal structure (Figure 8e$_2$) on the cell surface/EPS and the dark dendritic areas were also present inside the cell (Figure 8e$_1$,e$_3$,e$_4$). It can also be seen from Figure 8 that there are many more darker granular areas inside the cell at Mg/Ca molar ratios of 0, 6, 9, and 12 than those inside the cell cultivated in the liquid culture medium without any Ca^{2+} and Mg^{2+} ions. The ultra-thin slices of *B. subtilis* J2 bacteria were also analyzed by STEM (Figure 9). Figure 9a$_1$ shows that there was a layer of loose EPS enveloping the cell, and it can be seen from Figure 9a$_2$ that Ca^{2+} ions were present in/on the EPS and inside the cell. Figure 9b$_1$,b$_2$ also show that Mg^{2+} and Ca^{2+} were present in/on the cell surface/EPS and inside the cell.

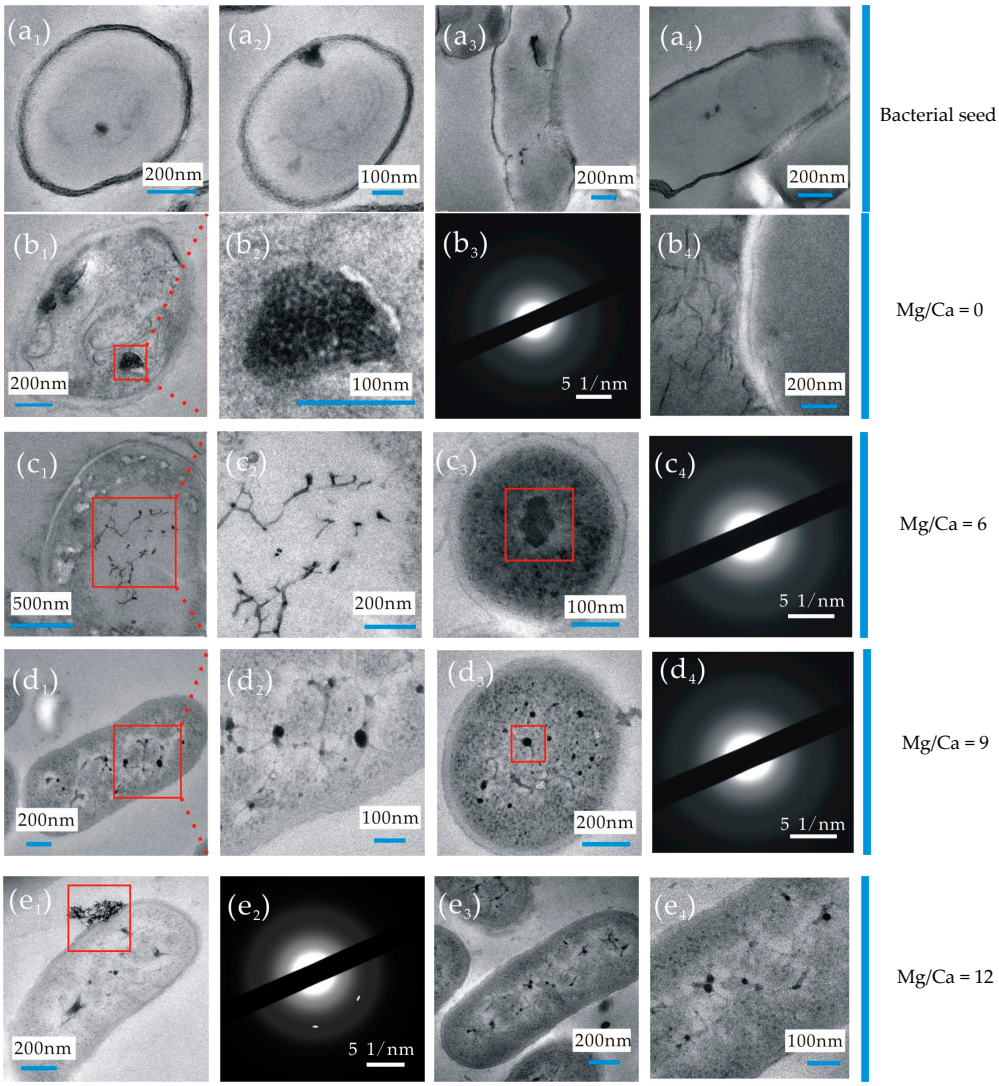

Figure 8. High-resolution transmission electron microscopy (HRTEM) and selected area electron diffraction (SAED) analyses of the ultra-thin slices of *B. subtilis* J2 bacteria.

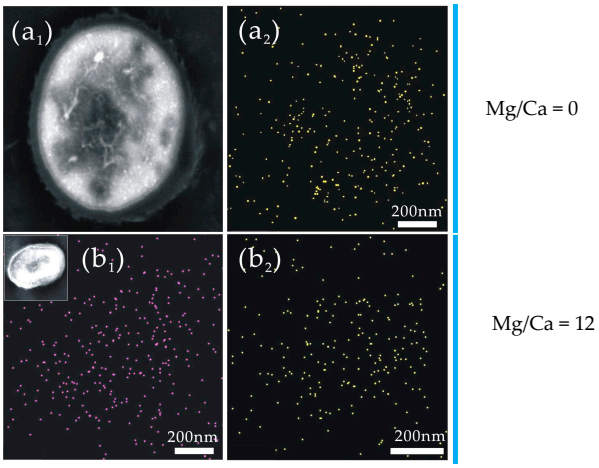

Figure 9. Bacterial ultra-thin slices analyzed by scanning transmission electron microscopy (STEM). Yellow and purple indicates Ca and Mg, respectively. (**a1**) bacterial ultra-thin slices analyzed by STEM; (**a2**) the distribution of Ca in/on the cell shown in (**a1**); (**b1**) the distribution of Ca in/on the cell shown in the inset; (**b2**) the distribution of Mg in/on the cell shown in the inset of (**b1**).

3.5. Amino Acids in EPS of B. subtilis J2

In this study, EPS were analyzed, and the results show that 17 kinds of amino acids were present (Figure 10). The molar ratio of glycine (Gly) was the highest, followed by aspartic acid (Asp) and alanine (Ala); the molar ratio of Asp was slightly higher than that of Ala (Figure 10). Among these 17 amino acids, the glutamate (Glu) content was also relatively high (Figure 10).

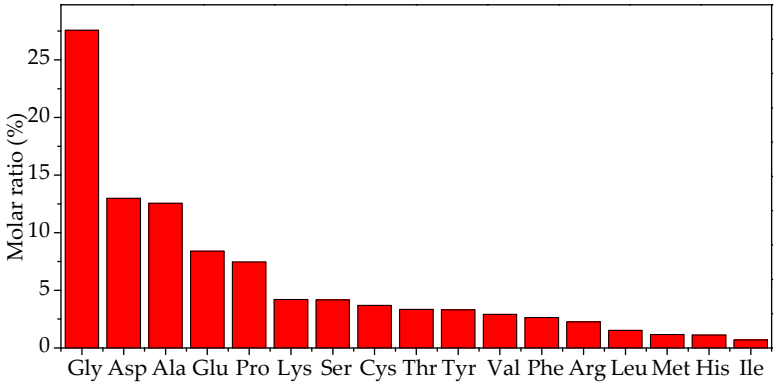

Figure 10. Amino acids in EPS secreted by *B. subtilis* J2 in the liquid culture medium.

4. Discussion

4.1. Mechanism of Biomineralization Induced by B. subtilis J2 Bacteria

4.1.1. Effects of NH_3 and CA on the pH Increase

It is well known that pH plays an important role in the biomineralization process induced by microorganisms, which can change the microenvironment around themselves by their own physiological and biochemical activities [41]. In this study, it was demonstrated that *B. subtilis* J2 bacteria can increase the pH to 9.22 in the liquid culture medium, and that without this bacterium, the pH value does not change but remains at 7.0 in the control group. This important result clearly shows that the pH increase is the consequence of the activities of the *B. subtilis* J2 bacteria. It has been reported that the main reason for the pH increase in the presence of bacteria is due to the ammonia released by the bacteria [94,95] according to the following reaction:

$$NH_3 + H_2O \rightarrow NH_4^+ + OH^- \quad (2)$$

and this result has been accepted for many years. However, in this study it was found that pH values still increased in the decline phase of the experiments, from 46 h to 195 h, and the pH remained at the maximum even when the bacterial cell concentration decreased to almost the minimum. This observation begs the question: Can microbes still produce ammonia during the microbial decline phase? If ammonia cannot continue to be produced, the increase in pH during the decline phase is not caused by ammonia. Thus, the quantity of ammonia released by the *B. subtilis* J2 bacteria was also investigated and the results show that, in the logarithmic growth stage, the bacteria did release a large amount of ammonia gas, resulting in an increase in pH, but in the decline phase, the bacteria produced almost no ammonia gas (Figure 3b). Thus, the pH increase in the decline phase was not due to the released ammonia because there was no ammonia released by *B. subtilis* J2 bacteria at this time. In fact, it can be observed that the quantity of ammonia was not high enough to make the pH increase to such a high degree (9.22) in the logarithmic growth stage, because the pH values based on the concentration of ammonia/ammonium were lower than those in the experimental group. Therefore, there must be other factors leading to the pH increase in the liquid culture medium.

Carbonic anhydrase was also investigated in this study and the results show that the pattern of CA change was similar to that of the growth curve. In the logarithmic growth stage, CA concentration

increased with an increase in the cell concentration, and then decreased slightly, and finally remained at 14.3 U/L. From these results, it can be concluded that CA can maintain a higher concentration even in the condition of a very low (the minimum) cell concentration in the bacterial decline phase, indicating that CA released by this bacterium was a type of continuously forming enzyme. The reason for a large value of CA still present in the decline phase was due to the fact that mRNA of CA was still stable and could be translated into the protein of the CA. For CA during a synchronous growth cycle of any organism, its mRNA would be degraded, and thus there would be no CA present in the decline phase. At the same time, as shown in Figure 3a–c, CA is also an alkaline enzyme because there is so much higher activity of CA even under alkaline conditions. In this study, due to the presence of alkaline CA, especially there were still a large number of CAs during the decline phase; the pH value in the liquid culture medium could easily increase. Alkaline CA can catalyze carbon dioxide hydration to release bicarbonate and carbonate ions and the reaction occurring was as follows:

$$CO_2 + H_2O \overset{CA}{\rightarrow} HCO_3^- + CO_3^{2-} \quad (3)$$

From this reaction, it can be inferred that there should be a large number of bicarbonate and carbonate ions present in the liquid culture medium by the catalysis of CA released from *B. subtills* J2 bacteria. This was the case. As shown in Figure 3c, a large number of bicarbonate and carbonate ions were indeed present in the liquid culture medium, and the occurrence of carbonate ions was later than that of the bicarbonate ions. The delay was due to the fact that the production of carbonate ions was the second step, which was based on the first step reaction, namely, hydrolysis of bicarbonate ions. That is to say, only when the bicarbonate ions reach a certain concentration can the concentration of carbonate ions be detected through the hydrolysis of bicarbonate ions. The sodium carbonate and sodium bicarbonate solution was prepared according to the concentration of the carbonate and bicarbonate ions, and pH values of the solution were also measured. As shown in Figure 3d, pH based on the concentration of the carbonate and bicarbonate ions increased to nearly 10.0, indicating that CA in this study could catalyze the carbon dioxide hydration to release a large number of bicarbonate and carbonate ions to increase pH values in the liquid culture medium. On the contrary, pH values based on the concentration of ammonium ions only increased to nearly 8.25 (Figure 3b), which was significantly lower than those in the experimental group ($p < 0.01$). Thus, the pH increase in this study was mainly due to the effect of CA combined with ammonia; it is possible that other factors were also involved in the pH increase. The reason for this pH increase will be further studied in future experiments.

4.1.2. The Second Role of CA Played in the Biomineralization

As explained above, the first role of CA is to catalyze the carbon dioxide hydration reaction to release a large number of bicarbonate and carbonate ions and further increase pH values in the culture medium. The second role of CA is that it can also elevate the supersaturation of some minerals in the liquid culture medium by releasing a large number of carbonate and bicarbonate ions; this role will also promote the precipitation of carbonate minerals such as calcite and aragonite. Under the effect of CA, the following reacton of calcium carbonate precipitation will proceed more quickly:

$$CO_3^{2-} + HCO_3^- + OH^- + 2Ca^{2+} \rightarrow 2CaCO_3 \downarrow + H_2O \quad (4)$$

As a result of the presence of enzymes, the free energy of the reaction is reduced and the reaction would proceed more quickly. It has been reported that CAs from three bacteria identified as *Bacillus* sp., *B. megaterium*, and *B. simplex* also play an important role in the process of calcium carbonate precipitation and the researchers have proposed that CA-producing microbes could be used as a sealing agent to fill gaps, cracks, and fissures in some building constructions [96]. The effect of bovine CA on the uptake rate of atmospheric carbon dioxide into solution has been examined, and the results have shown that CA can catalyze the hydration of aqueous carbon dioxide so that the uptake rates of carbon dioxide are accelerated up to 600% and 150%, compared to a control group. What is more, the precipitated

mineral was a Mg-carbonate and this can be effective as a means of sequestering carbon dioxide [97]. Some scientists have immobilized CA in alginate beads and further investigated its catalytic efficiency, and found that the entrapped CA hydrates carbon dioxide to bicarbonate and/or carbonate which can then react with Ca^{2+} ions to form calcite [98]. Thus, either free or immobilized CA could have a great potential for carbon dioxide sequestration through biomineralization processes.

The reaction of carbon dioxide hydration is very slow without CA catalysis [99]. It has been reported that CA is claimed to be one of the fastest reactive enzymes and the typical catalytic rate of different types of CAs can reach $10–10^6$ s^{-1} [100]. In our study, alkaline CA could also fix carbon dioxide and catalyze the production of bicarbonate and carbonate ions, and it further promoted the precipitation of carbonate minerals. However, no CA/bacteria were present in the control group, accounting for the fact that pH stayed at the same level all the time without any change. Without CA, carbon dioxide hydration was very slow and the concentration of bicarbonate and carbonate ions was too low to precipitate the minerals. In our opinion, if there were no bacteria, there would be far fewer carbonate minerals and deposits; in other words, microbialites would not be formed in nature.

4.2. The Nucleation Sites

In this study, the results of SEM and HRTEM analyses shown in Figures 5c_3,d_2 and 8e_1 showed that EPS were the nucleation sites for the precipitation of minerals and this opinion has been accepted by many scientists [101–108]. Sulphate-reducing bacteria (SRB) and halophilic bacteria have been used to induce the precipitation of dolomite [56], and the results have shown that these EPS-like materials may have served as an additional template for dolomite nucleation, since no dolomite was detected in experiments containing heat-killed bacteria due to the absence of EPS materials. In fact it is the structure of EPS that enables them to act as nucleation sites. Figure 10 shows that Glu and Asp were the amino acids with higher contents in EPS; in addition, these two amino acids are acidic amino acids and have two carboxyl groups. The two carboxyl groups have important roles: one is used to form the peptide bond and the other is free. It can be seen that if there was a large amount of Glu and Asp, which have two carboxyl groups to every one molecule, present in the EPS of *B. subtilis* J2 bacteria, there would be a lot of carboxyl groups in the EPS. From Figure 3a, the pH value was seen to have increased to 9.22 under the effect of *B. subtilis* J2 bacteria; in this highly alkaline condition, Glu and Asp would be deprotonated due to the fact that the isoelectric point (pI) values of Glu and Asp were 3.22 and 2.77, respectively, much lower than 9.22. That is to say, Glu and Asp would carry negative charges and this characteristic would be beneficial to the adsorbtion of Ca^{2+} and Mg^{2+} ions. Thus, it is not difficult to explain why the EPS show the presence of calcium and magnesium (Figure 9). Figure 6f–h show that there are some organic functional groups on/within the minerals, such as C–O–C, N–H, C=O, O–H, and C–H; these may be closely related to EPS components. In the meanwhile, carbonate and bicarbonate ions would be released in the processs of carbon dioxide hydration catalyzed by CA, and ammonia could also be produced to dissolve into the liquid culture medium to release the hydroxyl groups; therefore, due to the increase in the alkalinity and the supersaturation, calcium carbonate minerals were precipitated in/on the EPS of *B. subtilis* J2 bacteria. In this study, the HRTEM results shown in Figure 8d_3,e_1 reveal that the EPS were indeed the nucleation site. The FTIR results also show many other organic funtional groups on/within the minerals (Figure 6f–h), such as C–O–C, N–H, C=O, O–H, and C–H. Therefore, other organic substances could also affect the nucleation of carbonate minerals besides the amino acids. There are many unknown components existing on/in the EPS of *B. subtilis* J2, such that the mechanism of nucleation on/in the EPS needs to be further examined.

The mineral shell wrapping around the bacterium (Figure 5c_3) also indicated that the EPS acted as nucleation sites. In fact, the mineralized shells similar to these also occur in the natural environment. A large number of cone-shaped bundles formed by elongate crystallites within the mid to lower parts of a modern microbial mat have been reported [109]. There is one thing in common: a hole is also present in the center of the terminations of the cone-shaped bundles. It is possible that the cone-shaped bundles with holes are biomineralization products formed under the effects of bacteria.

4.3. Aragonite Minerals Induced by B. subtilis J2 Bacteria

In this study, aragonite was precipitated at Mg/Ca molar ratios of 3, 6, 9, and 12, and only calcite was formed at a Mg/Ca molar ratio of 0 in the experimental group; this indictates that Mg ions play an important role in the precipitation of aragonite. In the field of mechanics, the usual way to precipitate aragonite is to add a certain concentration of Mg^{2+} ions to the solution [110], also demonstrating the important role of Mg in the precipitation of aragonite. In our experiments, there were no minerals precipitated in the control group which had no bacteria, even at higher concentrations of Mg^{2+}; clearly indicating that there are other factors promoting the formation of aragonite besides the presence of Mg^{2+} ions. In our opinion, it was the *B. subtilis* J2 strain that promoted the precipitation of aragonite, since it not only released CA and ammonia to increase the alkalinity and supersaturation but also supplied nucleation sites for the precipitation of minerals. In this study, 17 amino acids were found to be present in/on the EPS. Amino acids are the basic building blocks of proteins and act as important factors in regulating the polymorphs and morphologies of calcium carbonate [111]. In vitro crystallization experiments, using matrix macromolecules (protein) extracted from the crossed lamellar layers of limpet shells, induced the formation of only aragonite minerals at a Ca/Mg ion ratio of 2:5 within 6 h [112]. It revealed the important role of the biomolecules and Mg^{2+} ions played in the precipitation of aragonite. In this study, there were a large number of mineral shells wrapping around spores and bacteria, similar to the shell of a mollusc scallop; this may indicate that the formation of the mineral shells is connected to the presence of biomolecules and Mg^{2+} ions. In the control group, without these biomolecules, no aragonite minerals were formed, even though the liquid culture medium reached saturation. It has also been reported that synthetic peptides (formed by amino acids) representing the 30 AA N- and C-terminal sequence regions of PFMG1 (a set of nacre protein sequences) can nucleate nanometer-size aragonite in a solution without additives [113]. The mechanism by which these peptides promote the nucleation of aragonite in vitro needs to be further explored.

In this study, the XRD results shown in Figure 4 reveal that the crystallinity of aragonite decreases with the increasing Mg^{2+} concentration, and DTG and DSC analyses also show that the thermal stability of aragonite decreases with an increase in the concentration of Mg^{2+} ions; these results suggest that Mg^{2+} ions affect the crystal structure of aragonite. Thus, the crystal structure of aragonite is being distorted, possibly due to the fact that the Ca atom is being replaced by the Mg atom in the biomineralization process. As for aragonite formed by physicochemical processes, Mg ions would be prevented from entering its lattice structure; whereas with the microbially induced aragonite, magnesium ions can usually enter its crystals easily. This is one of the characteristic features of aragonite induced by microorganisms.

5. Conclusions

In this study, the *B. subtilis* J2 bacterium was used in experiments to induce the precipitation of calcium carbonate at Mg/Ca molar ratios of 0, 3, 6, 9 and 12. The bacteria released CA and ammonia to increase the concentration of bicarbonate, carbonate, and hydroxyl ions in the solution, and these led to an increase in pH and elevation of the supersaturation in the liquid culture medium. The content of Mg in/on aragonite minerals increased with increasing Mg^{2+} concentration. The crystallinity and thermal stability of aragonite decreased with an increase in the Mg/Ca molar ratio, which may be due to the replacement of Ca atoms by Mg atoms. The FTIR results showed many organic funtional groups on/within the minerals, such as C–O–C, N–H, C=O, O–H, and C–H. The HRTEM-SAED observations of the ultra-thin slices of *B. subtilis* J2 bacteria showed there were nanoscale-sized minerals with poor crystal structures grown/adsorbed on the EPS. The EPS of the *B. subtilis* J2 strain were rich in Glu and Asp, which contained two carboxyl groups that could be deprotonated when pH exceeded their pIs; this made the EPS act as the nucleation sites. This study provides some insights for further understanding of the mechanisms of biomineralization induced by microorganisms.

Supplementary Materials: The following are available online at http://www.mdpi.com/2075-163X/9/4/218/s1, Figure S1: Images of the control groups A and B. (a) The image of control group A, pH was 7.00, and Mg/Ca ratio from left to right was 0,3,6,9, and 12, respectively. (b1) The image of control group B, pH was 9.20, and Mg/Ca ratio from left to right was 0,3,6,9, and 12, respectively. (b2) The image of control group B after centrifugation, pH was 9.20, and Mg/Ca ratio from left to right was 0,3,6,9, and 12, respectively. Figure S2. XRD analysis of the precipitates in the control groups B at pH 9.20 and Mg/Ca ratio of 0. Figure S3. SEM (a, b, c, and d) and EDS (e, f, and g) images of the precipitates in the control groups B at pH 9.20 and Mg/Ca ratio of 0. The elemental analysis of the area marked by the red square in figure a, b, and c was shown in e, f, and g, respectively.

Author Contributions: Z.H. and H.Y. conceived and designed the experiments; J.W., J.Z., and H.Z. (Hui Zhao) performed the experiments; H.Z. (Hui Zhao), X.Z., and H.Y. analyzed the results of all the experiments; Y.Z., G.W., H.Z. (Hucheng Zhang), and J.Y. were in charge of calculations; H.Y. and M.E.T. revised the manuscript. All authors read and approved the manuscript.

Funding: This work was supported by the Laboratory for Marine Mineral Resources, Qingdao National Laboratory for Marine Science and Technology, grant No. MMRZZ201804; the National Natural Science Foundation of China (41772095, U1663201, 41702131); Taishan Scholar Talent Team Support Plan for Advanced & Unique Discipline Areas, Major Scientific and Technological Innovation Projects of Shandong Province (2017CXGC1602, 2017CXGC1603); SDUST Research Fund (2015TDJH101); Natural Science Foundation of Shandong Province (ZR2017BD001); the China Postdoctoral Science Foundation founded project (2016M600548, 2017T100502); Qingdao Postdoctoral Applied Research Project (2015199); the Scientific and Technological Innovation Project Financially Supported by Qingdao National Laboratory for Marine Science and Technology (No. 2016ASKJ13); Open Fund of the Key Laboratory of Marine Geology and Environment, Chinese Academy of Sciences (No. MGE2016KG10); Postgraduate Science and Technology Innovation Project of Shandong University of Science and Technology (SDKDYC180105, SDKDYC180211); National College Students' Innovation and Entrepreneurship Training Program (201710424013, 201810424025).

Conflicts of Interest: The authors declare no conflicts of interest.

References

1. Lowenstam, H.A. Minerals formed by organisms. *Science* **1981**, *211*, 1126–1131. [CrossRef]
2. Weiner, S.; Dove, P.M. An overview of biomineralization processes and the problem of the vital effect. *Rev. Mineral. Geochem.* **2003**, *54*, 1–29. [CrossRef]
3. Chen, J.; Van Loon, A.J.; Han, Z.; Chough, S.K. Funnel-shaped, breccia-filled clastic dykes in the Late Cambrian Chaomidian Formation (Shandong Province, China). *Sediment. Geol.* **2009**, *221*, 1–6. [CrossRef]
4. Chen, J.; Chough, S.K.; Chun, S.S.; Han, Z. Limestone pseudoconglomerates in the Late Cambrian Gushan and Chaomidian Formations (Shandong Province, China): Soft-sediment deformation induced by storm-wave loading. *Sedimentology* **2010**, *56*, 1174–1195. [CrossRef]
5. Chen, J.; Han, Z.; Zhang, X.; Fan, A.; Yang, R. Early diagenetic deformation structures of the Furongian ribbon rocks in Shandong Province of China—A new perspective of the genesis of limestone conglomerates. *Sci. China Earth Sci.* **2010**, *53*, 241–252. [CrossRef]
6. Chen, J.; Chough, S.K.; Han, Z.; Lee, J.-H. An extensive erosion surface of a strongly deformed limestone bed in the Gushan and Chaomidian formations (late Middle Cambrian to Furongian), Shandong Province, China: Sequence-stratigraphic implications. *Sediment. Geol.* **2011**, *233*, 129–149. [CrossRef]
7. Chen, J.; Chough, S.K.; Lee, J.-H.; Han, Z. Sequence-stratigraphic comparison of the upper Cambrian Series 3 to Furongian succession between the Shandong region, China and the Taebaek area, Korea: High variability of bounding surfaces in an epeiric platform. *Geosci. J.* **2012**, *16*, 357–379. [CrossRef]
8. Lee, J.; Chen, J.; Choh, S.; Lee, D.; Han, Z.; Chough, S.K. Furongian (Late Cambrian) sponge–microbial maze-like reefs in the north china platform. *Palaios* **2001**, *29*, 27–37. [CrossRef]
9. Van Loon, A.J.T.; Han, Z.; Han, Y. Origin of the vertically orientated clasts in brecciated shallow-marine limestones of the Chaomidian Formation (Furongian, Shandong Province, China). *Sedimentology* **2013**, *60*, 1059–1070. [CrossRef]
10. Woo, J.; Chough, S.K.; Han, Z. Chambers of *Epiphyton thalli* in microbial buildups, Zhangxia Formation (Middle Cambrian), Shandong Province, China. *Palaios* **2008**, *23*, 55–64. [CrossRef]
11. Park, T.Y.; Sang, J.M.; Han, Z.; Choi, D.K. Ontogeny of the middle cambrian trilobite shantungia spinifera walcott, 1905 from north china and its taxonomic significance. *J. Paleontol.* **2008**, *82*, 851–855. [CrossRef]
12. Liu, Y.; Jiao, X.; Li, H.; Yuan, M.; Yang, W.; Zhou, X.; Liang, H.; Zhou, D.; Zheng, C.; Sun, Q.; et al. Primary dolostone formation related to mantle-originated exhalative hydrothermal activities, Permian Yuejingou section, Santanghu area, Xinjiang, NW China. *Sci. China Earth Sci.* **2012**, *55*, 183–192. [CrossRef]

13. Han, Z.; Zhang, X.; Chi, N.; Han, M.; Woo, J.; Lee, H.S.; Chen, J. Cambrian oncoids and other microbial-related grains on the North China Platform. *Carbonates Evaporites* **2015**, *30*, 373–386. [CrossRef]
14. Fan, A.; Yang, R.; van Loon, A.J.; Yin, W.; Han, Z.; Zavala, C. Classification of gravity-flow deposits and their significance for unconventional petroleum exploration, with a case study from the Triassic Yanchang Formation (southern Ordos Basin, China). *J. Asian Earth Sci.* **2018**, *161*, 57–73. [CrossRef]
15. Chang, X.; Wang, T.G.; Li, Q.; Cheng, B.; Tao, X. Geochemistry and possible origin of petroleum in Palaeozoic reservoirs from Halahatang Depression. *J. Asian Earth Sci.* **2013**, *74*, 129–141. [CrossRef]
16. Frankel, R.B.; Bazylinski, D.A. Biologically induced mineralization by bacteria. *Rev. Mineral. Geochem.* **2003**, *54*, 95–114. [CrossRef]
17. Chough, S.K.; Lee, H.S.; Woo, J.; Chen, J.; Choi, D.K.; Lee, S.-b.; Kang, I.; Park, T.-y.; Han, Z. Cambrian stratigraphy of the North China Platform: Revisiting principal sections in Shandong Province, China. *Geosci. J.* **2010**, *14*, 235–268. [CrossRef]
18. Lee, J.-H.; Chen, J.; Chough, S.K. Paleoenvironmental implications of an extensive maceriate microbialite bed in the Furongian Chaomidian Formation, Shandong Province, China. *Palaeogeogr. Palaeoclimatol. Palaeoecol.* **2010**, *297*, 621–632. [CrossRef]
19. Lv, D.; Chen, J. Depositional environments and sequence stratigraphy of the Late Carboniferous–Early Permian coal-bearing successions (Shandong Province, China): Sequence development in an epicontinental basin. *J. Asian Earth Sci.* **2014**, *79*, 16–30. [CrossRef]
20. Yin, S.; Lv, D.; Jin, L.; Ding, W. Experimental analysis and application of the effect of stress on continental shale reservoir brittleness. *J. Geophys. Eng.* **2018**, *15*, 478–494. [CrossRef]
21. Xu, Y.; Shen, X.; Chen, N.; Yang, C.; Wang, Q. Evaluation of reservoir connectivity using whole-oil gas chromatographic fingerprint technology: A case study from the Es_3^3 reservoir in the Nanpu Sag, China. *Pet. Sci. Technol.* **2012**, *9*, 290–294. [CrossRef]
22. Castanier, S.; Le Métayer-Levrel, G.; Perthuisot, J.-P. Ca-carbonates precipitation and limestone genesis—The microbiogeologist point of view. *Sediment. Geol.* **1999**, *126*, 9–23. [CrossRef]
23. Qiu, X.; Liu, C.; Mao, G.; Deng, Y.; Wang, F.; Wang, J. Late Triassic tuff intervals in the Ordos basin, Central China: Their depositional, petrographic, geochemical characteristics and regional implications. *J. Asian Earth Sci.* **2014**, *80*, 148–160. [CrossRef]
24. Yang, R.; van Loon, A.J.; Jin, X.; Jin, Z.; Han, Z.; Fan, A.; Liu, Q. From divergent to convergent plates: Resulting facies shifts along the southern and western margins of the Sino-Korean Plate during the Ordovician. *J. Geodyn.* **2018**. [CrossRef]
25. Zhang, X.; Feng, Q.; Sun, P.; Li, W. Characteristics of high gamma ray reservoir of Yanchang formation in Ordos basin. *Chin. J. Geophys-Chin. Ed.* **2010**, *53*, 205–213. [CrossRef]
26. Wang, Y.; Yang, R.; Song, M.; Lenhardt, N.; Wang, X.; Zhang, X.; Yang, S.; Wang, J.; Cao, H. Characteristics, controls and geological models of hydrocarbon accumulation in the Carboniferous volcanic reservoirs of the Chunfeng Oilfield, Junggar Basin, northwestern China. *Mar. Pet. Geol.* **2018**, *94*, 65–79. [CrossRef]
27. Xu, Y.; Lu, M. Microbially enhanced oil recovery at simulated reservoir conditions by use of engineered bacteria. *J. Pet. Sci. Eng.* **2011**, *78*, 233–238. [CrossRef]
28. Omar, N.B.; Arias, J.M.; Gonzalez-Munoz, M.T. Extracellular bacterial mineralization within the context of geomicrobiology. *Microbiologia* **1997**, *13*, 161–172. [PubMed]
29. Zhang, C.; Dehoff, K.; Hess, N.; Oostrom, M.; Wietsma, T.W.; Valocchi, A.J.; Fouke, B.W.; Werth, C.J. Pore-scale study of transverse mixing induced $CaCO_3$ precipitation and permeability reduction in a model subsurface sedimentary system. *Environ. Sci. Technol.* **2010**, *44*, 7833–7838. [CrossRef] [PubMed]
30. Tiano, P.; Biagiotti, L.; Mastromei, G. Bacterial bio-mediated calcite precipitation for monumental stones conservation: Methods of evaluation. *J. Microbiol. Meth.* **1999**, *36*, 139–145. [CrossRef]
31. Le Métayer-Levrel, G.; Castanier, S.; Orial, G.; Loubière, J.F.; Perthuisot, J.P. Applications of bacterial carbonatogenesis to the protection and regeneration of limestones in buildings and historic patrimony. *Sediment. Geol.* **1999**, *126*, 25–34. [CrossRef]
32. Bian, X.; Wang, Z.-f.; Ding, G.-q.; Cao, Y.-P. Compressibility of cemented dredged clay at high water content with super-absorbent polymer. *Eng. Geol.* **2016**, *208*, 198–205. [CrossRef]
33. Dhami, N.K.; Mukherjee, A. Carbonate biomineralization and heavy metal remediation by calcifying fungi isolated from karstic caves. *Ecol. Eng.* **2017**, *103*, 106–117. [CrossRef]

34. Kim, I.G.; Jo, B.H.; Kang, D.G.; Kim, C.S.; Choi, Y.S.; Cha, H.J. Biomineralization-based conversion of carbon dioxide to calcium carbonate using recombinant carbonic anhydrase. *Chemosphere* **2012**, *87*, 1091–1096. [CrossRef]
35. Lv, D.; Li, Z.; Chen, J.; Liu, H.; Guo, J.; Shang, L. Characteristics of the Permian coal-formed gas sandstone reservoirs in Bohai Bay Basin and the adjacent areas, North China. *J. Pet. Sci. Eng.* **2011**, *78*, 516–528. [CrossRef]
36. Yu, H.; Yuan, J.; Guo, W.; Cheng, J.; Hu, Q. A preliminary laboratory experiment on coalbed methane displacement with carbon dioxide injection. *Int. J. Coal. Geol.* **2008**, *73*, 156–166. [CrossRef]
37. Yu, H.; Zhou, G.; Fan, W.; Ye, J. Predicted CO_2 enhanced coalbed methane recovery and CO_2 sequestration in China. *Int. J. Coal Geol.* **2007**, *71*, 345–357. [CrossRef]
38. Yu, H.; Zhou, L.; Guo, W.; Cheng, J.; Hu, Q. Predictions of the adsorption equilibrium of methane/carbon dioxide binary gas on coals using Langmuir and ideal adsorbed solution theory under feed gas conditions. *Int. J. Coal Geol.* **2008**, *73*, 115–129. [CrossRef]
39. Wright, D.T.; Oren, A. Nonphotosynthetic Bacteria and the Formation of Carbonates and Evaporites Through Time. *Geomicrobiol. J.* **2005**, *22*, 27–53. [CrossRef]
40. Han, Z.; Gao, X.; Zhao, H.; Tucker, M.; Zhao, Y.; Bi, Z.; Pan, J.; Wu, G.; Yan, H. Extracellular and Intracellular Biomineralization Induced by *Bacillus licheniformis* DB1-9 at Different Mg/Ca Molar Ratios. *Minerals* **2018**, *8*, 585. [CrossRef]
41. Han, Z.; Li, D.; Zhao, H.; Yan, H.; Li, P. Precipitation of carbonate minerals induced by the Halophilic *Chromohalobacter Israelensis* under high salt concentrations: Implications for natural environments. *Minerals* **2017**, *7*, 95. [CrossRef]
42. Han, Z.; Meng, R.; Yan, H.; Zhao, H.; Han, M.; Zhao, Y.; Sun, B.; Sun, Y.; Wang, J.; Zhuang, D.; et al. Calcium carbonate precipitation by *Synechocystis* sp. PCC6803 at different Mg/Ca molar ratios under the laboratory condition. *Carbonates Evaporites* **2016**, *32*, 561–575. [CrossRef]
43. Han, Z.; Sun, B.; Zhao, H.; Yan, H.; Han, M.; Zhao, Y.; Meng, R.; Zhuang, D.; Li, D.; Ma, Y.; et al. Isolation of *Leclercia adcarboxglata* Strain JLS1 from dolostone sample and characterization of its induced struvite minerals. *Geomicrobiol. J.* **2017**, *34*, 500–510. [CrossRef]
44. Yan, H.; Han, Z.; Zhao, H.; Zhou, S.; Chi, N.; Han, M.; Kou, X. Characterization of calcium deposition induced by *Synechocystis* sp. PCC6803 in BG11 culture medium. *Chin. J. Oceanol. Limnol.* **2014**, *32*, 503–510. [CrossRef]
45. Han, Z.; Yan, H.; Zhou, S.; Zhao, H.; Zhang, Y.; Zhang, N.; Yao, C.; Zhao, L.; Han, C. Precipitation of calcite induced by *Synechocystis* sp. PCC6803. *World J. Microbiol. Biotechnol.* **2013**, *29*, 1801–1811. [CrossRef]
46. Han, Z.; Yan, H.; Zhao, H.; Zhou, S.; Han, M.; Meng, X.; Zhang, Y.; Zhao, Y.; Sun, B.; Yao, C.; et al. Bio-precipitation of calcite with preferential orientation induced by *Synechocystis* sp. PCC6803. *Geomicrobiol. J.* **2014**, *31*, 884–899. [CrossRef]
47. Han, Z.; Yu, W.; Zhao, H.; Zhao, Y.; Tucker, M.; Yan, H. The Significant Roles of Mg/Ca Ratio, Cl^- and SO_4^{2-} in Carbonate Mineral Precipitation by the Halophile *Staphylococcus epidermis* Y2. *Minerals* **2018**, *8*, 594. [CrossRef]
48. Han, Z.; Zhao, Y.; Yan, H.; Zhao, H.; Han, M.; Sun, B.; Sun, X.; Hou, F.; Sun, H.; Han, L.; et al. Struvite precipitation induced by a novel Sulfate-Reducing Bacterium *Acinetobacter calcoaceticus* SRB4 isolated from river sediment. *Geomicrobiol. J.* **2015**, *32*, 868–877. [CrossRef]
49. Han, Z.; Zhao, Y.; Yan, H.; Zhao, H.; Han, M.; Sun, B.; Meng, R.; Zhuang, D.; Li, D.; Gao, W.; et al. The Characterization of Intracellular and Extracellular Biomineralization Induced by *Synechocystis* sp. PCC6803 Cultured under Low Mg/Ca Ratios Conditions. *Geomicrobiol. J.* **2017**, *34*, 362–373. [CrossRef]
50. Han, M.; Zhao, Y.; Zhao, H.; Han, Z.; Yan, H.; Sun, B.; Meng, R.; Zhuang, D.; Li, D.; Liu, B. A comparison of amorphous calcium carbonate crystallization in aqueous solutions of $MgCl_2$ and $MgSO_4$: Implications for paleo-ocean chemistry. *Miner. Pet.* **2018**, *112*, 229–244. [CrossRef]
51. Zhuang, D.; Yan, H.; Tucker, M.E.; Zhao, H.; Han, Z.; Zhao, Y.; Sun, B.; Li, D.; Pan, J.; Zhao, Y.; et al. Calcite precipitation induced by *Bacillus cereus* MRR2 cultured at different Ca^{2+} concentrations: Further insights into biotic and abiotic calcite. *Chem. Geol.* **2018**, *500*, 64–87. [CrossRef]
52. Han, Z.; Zhuang, D.; Yan, H.; Zhao, H.; Sun, B.; Li, D.; Sun, Y.; Hu, W.; Xuan, Q.; Chen, J.; et al. Thermogravimetric and kinetic analysis of thermal decomposition characteristics of microbial calcites induced by *cyanobacteria Synechocystis* sp. PCC6803. *J. Therm. Anal. Calorim.* **2017**, *127*, 1371–1379. [CrossRef]

53. Ma, P.; Wang, C.; Lv, D.; Li, Y.; Yi, L. Controls on deposition of aquatic and terrestrial organic matter in the lacustrine Namling–Oiyug basin (Oligocene–Miocene, southern Tibet). *Int. J. Coal Geol.* **2015**, *149*, 108–117. [CrossRef]
54. Grasby, S.E. Naturally precipitating vaterite (μ-CaCO3) spheres: Unusual carbonates formed in an extreme environment. *Geochim. Cosmochim. Acta* **2003**, *67*, 1659–1666. [CrossRef]
55. Castanier, S.; Métayer-Levrel, G.L.; Perthuisot, J.-P. Bacterial Roles in the Precipitation of Carbonate Minerals. In *Microbial Sediments*; Riding, R.E., Awramik, S.M., Eds.; Springer: Berlin/Heidelberg, Germany, 2000; pp. 32–39. [CrossRef]
56. Deng, S.; Dong, H.; Lv, G.; Jiang, H.; Yu, B.; Bishop, M.E. Microbial dolomite precipitation using sulfate reducing and halophilic bacteria: Results from Qinghai Lake, Tibetan Plateau, NW China. *Chem. Geol.* **2010**, *278*, 151–159. [CrossRef]
57. Kim, C.S.; Lee, C.H.; Shin, J.S.; Chung, Y.S.; Hyung, N.I. A simple and rapid method for isolation of high quality genomic DNA from fruit trees and conifers using PVP. *Nucleic Acids Res.* **1997**, *25*, 1085–1086. [CrossRef] [PubMed]
58. Madhaiyan, M.; Poonguzhali, S.; Kwon, S.-W.; Sa, T.-M. Methylobacterium *phyllosphaerae* sp. nov., a pink-pigmented, facultative methylotroph from the phyllosphere of rice. *Int. J. Syst. Evol. Microbiol.* **2009**, *59*, 22–27. [CrossRef]
59. Li, Z.; Hao, A.; Li, X. β-Cyclodextrin supramolecular organogels induced by different carboxylic acids that exhibit diverse morphologies. *J. Mol. Liq.* **2014**, *196*, 52–60. [CrossRef]
60. Jiang, N.; Zhao, L.F.; Gan, Z.H. Influence of nucleating agent on the formation and enzymatic degradation of poly(butylene adipate) polymorphic crystals. *Polym. Degrad. Stabil.* **2010**, *95*, 1045–1053. [CrossRef]
61. Wang, J.; Chen, D.; Xu, Y.; Liu, Q.; Zhang, L. Influence of the crystal texture on raman spectroscopy of the ALN films prepared by pulse laser deposition. *J. Spectrosc.* **2013**. [CrossRef]
62. Guo, J.; Li, X.; Sun, Y.; Liu, Q.; Quan, Z.; Zhang, X. In-situ confined formation of NiFe layered double hydroxide quantum dots in expanded graphite for active electrocatalytic oxygen evolution. *J. Solid State Chem.* **2018**, *262*, 181–185. [CrossRef]
63. Hou, Q.; Ren, J.; Chen, H.; Yang, P.; Shao, Q.; Zhao, M.; Zhao, X.; He, H.; Wang, N.; Luo, Q.; et al. Synergistic Hematite-Fullerene Electron-Extracting Layers for Improved Efficiency and Stability in Perovskite Solar Cells. *ChemElectroChem* **2018**, *5*, 726–731. [CrossRef]
64. Meng, T.-H.; Zhou, Y.; Gao, Z.-Z.; Liu, Q.-Y.; Tao, Z.; Xiao, X. A study of the inclusion of 1-hexyl-4-(4-pyridyl)pyridinium bromide in cucurbit [6] uril. *J. Incl. Phenom. Macrocycl. Chem.* **2018**, *90*, 357–363. [CrossRef]
65. Wang, Y.; Zhang, X.; Liu, X.; Bai, W.; Zhu, Z.; Wang, Y.; Gao, J. Control of extractive distillation process for separating heterogenerous ternary azeotropic mixture via adjusting the solvent content. *Sep. Purif. Technol.* **2018**, *191*, 8–26. [CrossRef]
66. Zhang, Y.; Li, H.; Zhang, Y.; Song, F.; Cao, X.; Lyu, X.; Zhang, Y.; Crittenden, J. Statistical optimization and batch studies on adsorption of phosphate using Al-eggshell. *Adsorpt. Sci. Technol.* **2017**, *36*, 999–1017. [CrossRef]
67. Zhao, B.; Shao, Q.; Hao, L.; Zhang, L.; Liu, Z.; Zhang, B.; Ge, S.; Guo, Z. Yeast-template synthesized Fe-doped cerium oxide hollow microspheres for visible photodegradation of acid orange 7. *J. Colloid Interf. Sci* **2018**, *511*, 39–47. [CrossRef]
68. Zhao, J.; Ge, S.; Liu, L.; Shao, Q.; Mai, X.; Xinxin Zhao, C.; Hao, L.; Wu, T.; Yu, Z.; Guo, Z. Microwave solvothermal fabrication of zirconia hollow microspheres with different morphologies using pollen templates and their dye adsorption removal. *Ind. Eng. Chem. Res.* **2017**, *57*, 231–241. [CrossRef]
69. Zhang, X.Y.; Ge, S.-S.; Shao, Q.; Liu, M.; Liu, Q.Y. Synthesis and Photocatalytic Activity of CeO_2 Hollow Microspheres via Yeast Template Route. *Chin. J. Inorg. Chem.* **2016**. [CrossRef]
70. Ning, Z.-b.; Nielsen, R.; Zhao, L.-f.; Yu, D.-h.; Gan, Z.-h. Influence of Teflon substrate on crystallization and enzymatic degradation of polymorphic poly(butylene adipate). *Chin. J. Polym. Sci.* **2014**, *32*, 1243–1252. [CrossRef]
71. Kang, H.; Cheng, Z.; Lai, H.; Ma, H.; Liu, Y.; Mai, X.; Wang, Y.; Shao, Q.; Xiang, L.; Guo, X.; et al. Superlyophobic anti-corrosive and self-cleaning titania robust mesh membrane with enhanced oil/water separation. *Sep. Purif. Technol.* **2018**, *201*, 193–204. [CrossRef]
72. Li, J.; Xia, J.; Zhang, F.; Wang, Z.; Liu, Q. An electrochemical sensor based on copper-based metal-organic frameworks-graphene composites for determination of dihydroxybenzene isomers in water. *Talanta* **2018**, *181*, 80–86. [CrossRef] [PubMed]

73. Li, J.; Xia, J.; Zhang, F.; Wang, Z.; Liu, Q. A novel electrochemical sensor based on copper-based metal-organic framework for the determination of dopamine. *J. Chin. Chem. Soc.* **2018**, *65*, 743–749. [CrossRef]
74. Tian, J.; Shao, Q.; Dong, X.; Zheng, J.; Pan, D.; Zhang, X.; Cao, H.; Hao, L.; Liu, J.; Mai, X.; et al. Bio-template synthesized NiO/C hollow microspheres with enhanced Li-ion battery electrochemical performance. *Electrochim. Acta* **2018**, *261*, 236–245. [CrossRef]
75. Wang, Z.; Yu, G.; Xia, J.; Zhang, F.; Liu, Q. One-step synthesis of a Methylene Blue@ZIF-8-reduced graphene oxide nanocomposite and its application to electrochemical sensing of rutin. *Microchim. Acta* **2018**, *185*, 279. [CrossRef] [PubMed]
76. Zhou, K.; Wang, X.; Ma, Z.; Lu, X.; Wang, Z.; Wang, L. Preparation and characterization of modified polyvinylidene fluoride/2-amino-4-thiazoleacetic acid ultrafiltration membrane for purification of Cr(VI) in water. *J. Chem. Eng. Jpn.* **2018**, *51*, 501–506. [CrossRef]
77. Tian, B.; Qiao, Y.y.; Tian, Y.y.; Xie, K.c.; Liu, Q.; Zhou, H.f. FTIR study on structural changes of different–rank coals caused by single/multiple extraction with cyclohexanone and NMP/CS_2 mixed solvent. *Fuel Process. Technol.* **2016**, *154*, 210–218. [CrossRef]
78. Li, T.; Yuan, C.; Zhao, Y.; Chen, Q.; Wei, M.; Wang, Y. Facile synthesis and characterization of poly (o-phenylenediamine) submicrospheres doped with glycine. *J. Macromol. Sci. A* **2013**, *50*, 330–333. [CrossRef]
79. Al, H.M.; Liu, Q. Ultrasound-Assisted Synthesis of Acylals Catalyzed by Stannum (IV) Phosphomolybdate under Solvent-Free Condition. *J. Chem. Soc. Pak.* **2012**, *34*, 299–301.
80. Zhao, H.; Yan, H.; Dong, S.; Zhang, Y.; Sun, B.; Zhang, C.; Ai, Y.; Chen, B.; Liu, Q.; Sui, T.; et al. Thermogravimetry study of the pyrolytic characteristics and kinetics of macro-algae Macrocystis pyrifera residue. *J. Therm. Anal. Calorim.* **2013**, *111*, 1685–1690. [CrossRef]
81. Zhao, H.; Yan, H.; Zhang, C.; Sun, B.; Zhang, Y.; Dong, S.; Xue, Y.; Qin, S. Thermogravimetry study of pyrolytic characteristics and kinetics of the giant wetland plant Phragmites australis. *J. Therm. Anal. Calorim* **2012**, *110*, 611–617. [CrossRef]
82. He, M.; Jin, H.; Zhang, L.; Jiang, H.; Yang, T.; Cui, H.; Fossard, F.; Wagner, J.B.; Karppinen, M.; Kauppinen, E.I.; et al. Environmental transmission electron microscopy investigations of Pt-Fe_2O_3 nanoparticles for nucleating carbon nanotubes. *Carbon* **2016**, *110*, 243–248. [CrossRef]
83. Hu, L.; Zhou, C.; Zhang, C.; Yue, Y. Thermodynamic anomaly of the sub-T(g) relaxation in hyperquenched metallic glasses. *J. Chem. Phys.* **2013**, *138*, 174508. [CrossRef]
84. Zhao, L.-f.; Li, Q.; Zhang, R.-l.; Tian, X.-j.; Liu, L. Effects of functionalized graphenes on the isothermal crystallization of poly(L-lactide) nanocomposites. *Chin. J. Polym. Sci.* **2016**, *34*, 111–121. [CrossRef]
85. Ding, J.; Zhao, Y.; Cui, H.; Gu, Y.; Wang, Y.; Liu, H.; Xu, G.; Han, Y. Appearance of [110] orientated growth layer on (100) face and exposure of (111) faces of cubic bismuth phosphate crystal. *J. Cryst. Growth* **2015**, *426*, 248–254. [CrossRef]
86. Qing, L.; Hong Mei, A. Ultrasound Promoted Synthesis of Arylmethylenemalonitriles Catalyzed by Melamine. *J. Chem. Soc. Pak.* **2016**, *38*, 565–569.
87. Zhao, L.F.; Jiang, N.; Gan, Z.H. Polymorphic Crystals from Different Thermal Treatments and Its Effect on Biodegradation Behavior of Poly(butylene adipate). *Chem. J. Chin. Univ.* **2011**, *32*, 185–189.
88. Zhao, L.; Tian, X.; Liu, X.; He, H.; Zhang, J.; Zhang, R. Miscibility and Isothermal Crystallization Behavior of Poly (Butylene Succinate-co-Adipate) (PBSA)/Poly (Trimethylene Carbonate) (PTMC) Blends. *J. Macromol. Sci. B* **2016**, *55*, 591–604. [CrossRef]
89. Wang, Z.W.; Zhong, X.S.; Wang, P.; Zhao, J.J.; Li, Y. Synthesis and Crystal Structure of 1D Gadolinium(III) Coordination Polymer Based on 5-Oxyacetate Isophthalic Acid. *Chin. J. Inorg. Chem.* **2011**, *27*, 1581–1585.
90. Liu, X.; Shao, X.; Fang, G.; He, H.; Wan, Z. Preparation and properties of chemically reduced graphene oxide/copolymer-polyamide nanocomposites. *e-Polymers* **2017**, *17*, 3–14. [CrossRef]
91. Kalmar, L.; Homola, D.; Varga, G.; Tompa, P. Structural disorder in proteins brings order to crystal growth in biomineralization. *Bone* **2012**, *51*, 528–534. [CrossRef]
92. Aizenberg, J.; Lambert, G.; Weiner, S.; Addadi, L. Factors Involved in the Formation of Amorphous and Crystalline Calcium Carbonate: A Study of an Ascidian Skeleton. *J. Am. Chem. Soc.* **2002**, *124*, 32–39. [CrossRef]
93. Albeck, S.; Addadi, L.; Weiner, S. Regulation of Calcite Crystal Morphology by Intracrystalline Acidic Proteins and Glycoproteins. *Connect. Tissue Res.* **1996**, *35*, 365–370. [CrossRef]

94. Baskar, S.; Routh, J.; Baskar, R.; Kumar, A.; Miettinen, H.; Itävaara, M. Evidences for Microbial Precipitation of Calcite in Speleothems from Krem Syndai in Jaintia Hills, Meghalaya, India. *Geomicrobiol. J.* **2016**, *33*, 906–933. [CrossRef]
95. Helmi, F.M.; Elmitwalli, H.R.; Elnagdy, S.M.; El-Hagrassy, A.F. Calcium carbonate precipitation induced by ureolytic bacteria *Bacillus licheniformis*. *Ecol. Eng.* **2016**, *90*, 367–371. [CrossRef]
96. Achal, V.; Pan, X. Characterization of Urease and Carbonic Anhydrase Producing Bacteria and Their Role in Calcite Precipitation. *Curr. Microbiol.* **2011**, *62*, 894–902. [CrossRef]
97. Power, I.M.; Harrison, A.L.; Dipple, G.M.; Southam, G. Carbon sequestration via carbonic anhydrase facilitated magnesium carbonate precipitation. *Int. J. Greenh. Gas Control* **2013**, *16*, 145–155. [CrossRef]
98. Yadav, R.R.; Mudliar, S.N.; Shekh, A.Y.; Fulke, A.B.; Devi, S.S.; Krishnamurthi, K.; Juwarkar, A.; Chakrabarti, T. Immobilization of carbonic anhydrase in alginate and its influence on transformation of CO_2 to calcite. *Process. Biochem.* **2012**, *47*, 585–590. [CrossRef]
99. Thatcher, B.J.; Doherty, A.E.; Orvisky, E.; Martin, B.M.; Henkin, R.I. Gustin from Human Parotid Saliva Is Carbonic Anhydrase VI. *Biochem. Biophys. Res. Commun.* **1998**, *250*, 635–641. [CrossRef]
100. Lindskog, S. Structure and mechanism of carbonic anhydrase. *Pharmacol. Therapeut.* **1997**, *74*, 1–20. [CrossRef]
101. Van Lith, Y.; Warthmann, R.; Vasconcelos, C.; McKenzie, J.A. Microbial fossilization in carbonate sediments: A result of the bacterial surface involvement in dolomite precipitation. *Sedimentology* **2003**, *50*, 237–245. [CrossRef]
102. Sánchez-Román, M.; Vasconcelos, C.; Schmid, T.; Dittrich, M.; McKenzie, J.A.; Zenobi, R.; Rivadeneyra, M.A. Aerobic microbial dolomite at the nanometer scale: Implications for the geologic record. *Geology* **2008**, *36*, 879–882. [CrossRef]
103. Bontognali, T.R.R.; Vasconcelos, C.; Warthmann, R.J.; Dupraz, C.; Bernasconi, S.M.; McKenzie, J.A. Microbes produce nanobacteria-like structures, avoiding cell entombment. *Geology* **2008**, *36*, 663–666. [CrossRef]
104. Bontognali, T.R.R.; Vasconcelos, C.; Warthmann, R.J.; Bernasconi, S.M.; Dupraz, C.; Strohmenger, C.J.; McKenzie, J.A. Dolomite formation within microbial mats in the coastal sabkha of Abu Dhabi (United Arab Emirates). *Sedimentology* **2010**, *57*, 824–844. [CrossRef]
105. Marvasi, M.; Casillas-Santiago, L.M.; Henríquez, T.; Casillas-Martinez, L. Involvement of *etfA* gene during $CaCO_3$ precipitation in *Bacillus subtilis* biofilm. *Geomicrobiol. J.* **2017**, *34*, 722–728. [CrossRef]
106. Marvasi, M.; Visscher, P.T.; Perito, B.; Mastromei, G.; Casillas-Martinez, L. Physiological requirements for carbonate precipitation during biofilm development of *Bacillus subtilis etfA* mutant. *FEMS Microbiol. Ecol.* **2010**, *71*, 341–350. [CrossRef]
107. Perito, B.; Casillas, L.; Marvasi, M. Factors affecting formation of large calcite crystals (≥1 mm) in *Bacillus subtilis* 168 biofilm. *Geomicrobiol. J.* **2018**, *35*, 385–391. [CrossRef]
108. Perito, B.; Marvasi, M.; Barabesi, C.; Mastromei, G.; Bracci, S.; Vendrell, M.; Tiano, P. A *Bacillus subtilis* cell fraction (BCF) inducing calcium carbonate precipitation: Biotechnological perspectives for monumental stone reinforcement. *J. Cult. Herit.* **2014**, *15*, 345–351. [CrossRef]
109. Perri, E.; Tucker, M.; Slowakiewicz, M.; Whitaker, F.; Bowen, L.; Perrotta, I. Carbonate and silicate biomineralization in a hypersaline microbial mat (Mesaieed sabkha, Qatar): Roles of bacteria, extracellular polymeric substances and viruses. *Sedimentology* **2017**, *65*. [CrossRef]
110. Nassif, N.; Gehrke, N.; Pinna, N.; Shirshova, N.; Tauer, K.; Antonietti, M.; Cölfen, H. Synthesis of Stable Aragonite Superstructures by a Biomimetic Crystallization Pathway. *Angew. Chem. Int. Edit.* **2005**, *44*, 6004–6009. [CrossRef]
111. Xie, A.-j.; Shen, Y.-h.; Li, X.-y.; Yuan, Z.-w.; Qiu, L.-g.; Zhang, C.-y.; Yang, Y.-f. The role of Mg^{2+} and Mg^{2+}/amino acid in controlling polymorph and morphology of calcium carbonate crystal. *Mater. Chem. Phys.* **2007**, *101*, 87–92. [CrossRef]
112. Suzuki, M.; Kogure, T.; Weiner, S.; Addadi, L. Formation of Aragonite Crystals in the Crossed Lamellar Microstructure of Limpet Shells. *Cryst. Growth Des.* **2011**, *11*, 4850–4859. [CrossRef]
113. Amos, F.F.; Destine, E.; Ponce, C.B.; Spencer Evans, J. The N- and C-terminal regions of the pearl-associated ef hand protein, pfmg1, promote the formation of the aragonite polymorph in vitro. *Cryst. Growth Des.* **2010**, *10*. [CrossRef]